Bárbara Maria Teixeira Costa Peluzo

AB-INITIO STUDIES OF Zr-Fe INTERMETALLICS AND THEIR HYDRIDES

ESTUDO *AB-INITIO* DE INTERMETÁLICOS DE Zr-Fe E SEUS HIDRETOS

CAMPINAS

2020

Bárbara Maria Teixeira Costa Peluzo

AB-INITIO STUDIES OF Zr-Fe INTERMETALLICS AND THEIR HYDRIDES

ESTUDO AB-INITIO DE INTERMETÁLICOS DE Zr-Fe E SEUS HIDRETOS

Dissertação apresentada ao Instituto de Física "Gleb Wataghin" da Universidade Estadual de Campinas como parte dos requisitos para a obtenção do título de Mestra em Física, na área de Física.

Dissertation presented to the "Gleb Wataghin" Institute of Physics of the University of Campinas in partial fulfillment of the requirements for the degree of Master in Physics, in the field of Physics.

Advisor/Orientador: Prof. Dr. Silvio Antonio Sachetto Vitiello

Este exemplar corresponde à versão final da Dissertação defendida por Bárbara Maria Teixeira Costa Peluzo e orientada pelo Prof. Dr. Silvio Antonio Sachetto Vitiello.

CAMPINAS

2020

MEMBROS DA COMISSÃO JULGADORA DA DISSERTAÇÃO DE MESTRADO DE BÁRBARA MARIA TEIXEIRA COSTA PELUZO – RA 211784 APRESENTADA E APROVADA AO INSTITUTO DE FÍSICA "GLEB WATAGHIN", DA UNIVERSIDADE ESTADUAL DE CAMPINAS, EM 21/07/2020.

COMISSÃO JULGADORA:

- Prof. Dr. Silvio Antonio Sachetto Vitiello – Orientador – DFMC/IFGW/UNICAMP

- Prof. Dr. Marcus Aloizio Martinez de Aguiar - DFMC/IFGW/UNICAMP

- Prof. Dr. Sebastian Ujevic Tonino - UFF

OBS.: Ata da defesa com as respectivas assinaturas dos membros encontra-se no SIGA/Sistema de Fluxo de Dissertação/Tese e na Secretaria do Programa da Unidade.

CAMPINAS

2020

Dedicatória

À minha família, em especial à minha mãe Mônica.

Vita brevis,
ars longa,
occasio praeceps,
experimentum periculosum,
iudicium difficile.

(Hippocrates)

Agradecimentos

Resumo

Neste trabalho, nosso objetivo é aplicar as metodologias da Teoria do Funcional da Densidade (DFT) e do método Variacional de Monte Carlo (VMC) no estudo dos intermetálicos Zr_2Fe e Zr_3Fe. Em um primeiro estágio, cálculos de DFT são empregados para obter a geometria de equilíbrio de cada liga e suas energias de coesão. Posteriormente, os orbitais de DFT são utilizados para construir um determinante de Slater e formar as funções de onda tentativa para cálculos de VMC. As correlações são incluídas através de termos de um e dois corpos no fator de Jastrow. Efeitos de tamanho são analisados através do emprego de 2 tamanhos de células de simulação, para cada sistema em estudo.

De forma geral, os resultados obtidos por DFT apresentam uma boa concordância em relação a trabalhos anteriores e razoável (dentro dos limites da DFT) em relação aos dados experimentais. As entalpias de formação das ligas foram comparadas com os dados experimentais, através da extrapolação dos resultados teóricos para 298 K, temperatura a qual estas reações ocorrem.

Os hidretos não possuem seus calores específicos reportados, portanto seus resultados não foram extrapolados. Contudo, devido ao fato de que há poucos estudos abordando estes sistemas, acreditamos que os resultados aqui reportados possam ser utilizados como ponto de partida para estudos mais acurados, como o método de Difusão de Monte Carlo, com o objetivo de investigar as propriedades destes sistemas.

Palavras-chave: Teoria do Funcional da Densidade. Monte Carlo Variacional. Zr-Fe

Abstract

In this work, our objective is to apply the Density Functional Theory (DFT) and Variational Monte Carlo (VMC) methodologies on the study of Zr_2Fe and Zr_3Fe intermetallics and their hydrides. At a first stage, DFT calculations are employed to achieve each alloy equilibrium geometry and their cohesive energies. Then, DFT orbitals are used to construct the Slater-Determinant and form the trial wave functions for VMC calculations. Correlations are included in one- and two-body terms in the Jastrow factor. Finite-size effects are investigated through the use of smaller and larger simulation cells.

In general, the DFT related results present good agreement with published data and a reasonable agreement (inside the DFT limitations) with the experimental ones. The alloys enthalpies of formation were compared with the experimental data, through the extrapolation of the theoretical results to 298 K, temperature in which the reactions occur.

The hydrides present a lack of information about their specific heats, thus their results could not be extrapolated. However, since there is a few studies about those systems, we believe that our results could be used as a starting point for a more accurate method, such as the Difusion Monte Carlo, in order to investigate these systems properties.

Key-words: Density Functional Theory. Variational Monte Carlo. Zr-Fe

List of Figures

List of Tables

List of Abbreviations

BOA	Born-Oppenheimer Approximation
BZ	Brillouin Zone
DFT	Density Functional Theory
DMC	Difusion Monte Carlo
EA	Electron Affinity
FU	Formation Unit
GGA	Generalized Density Approximation
ICSD	Inorganic Crystal Structure Database
IP	Ionization Potential
LDA	Local Density Approximation
NCPP	Norm Conserving Pseudopotential
PBE	Perdew-Burke-Ernzerhof
PES	Potential Energy Surface
QMC	Quantum Monte Carlo
RRKJ	Rappe-Rabe-Kaxiras-Joannopoulos
SC	Supercell
USPP	Ultrasoft Pseudopotentials
VMC	Variational Monte Carlo

List of Symbols

N Total electrons number. Number of samplings in the Metropolis Algorithm

M Total atoms number. Total number of variational parameters in one- and two-body Jastrow factors.

$\Phi(\{\mathbf{r}\}, \{\mathbf{R}\})$ Global wave function

$\Psi(\{\mathbf{r}\}; \{\mathbf{R}\})$ Electronic wave function

$\Psi(\{\mathbf{r}\})$ Reduced notation for the electronic wave function

$\Theta(\{\mathbf{R}\})$ Nuclear wave function

ε_{elec} Energy associated with the electronic Hamiltonian

ε_{tot} A system total (electronic + nuclear) energy

H_{elec} Electronic Hamiltonian

H_{nucl} Nuclear Hamiltonian

H Hamiltonian operator

Z_A Atomic number for atom A

r_{iA} Distance between atom A and electron i

r_{ij} Distance between electrons i and j

R_{AB} Distance between nuclei A and B

$\psi(\mathbf{r})$ Single-particle wave function

$\alpha(\sigma)$ Spin function

$\beta(\sigma)$ Spin function

σ Spin variable

ψ_v Valence orbital

ψ_c Core orbital

φ_v Pseudo wave function

E_v Energy eigenvalue for ψ_v

E_c Energy eigenvalue for ψ_c

V^{PP} Pseudopotential

r_c Core radius for a pseudopotential. Cut-off distance for a Jastrow factor.

$F_l(r)$ Term on the pseudo wave function in RRKJ pseudopotential

$C_l(r)$ Correction term on the pseudo wave function if RRKJ pseudopotential

$j_l(r, k_i)$ Bessel function

a_i Coefficients for Bessel functions in RRKJ pseudopotential

$n(\mathbf{r})$ Electronic density

$E[n(\mathbf{r})\ ]$ Total energy in DFT formalism

$T[n(\mathbf{r})\ ]$ Kinetic energy contribution in DFT formalism

$U_{ee}[n(\mathbf{r})\ ]$ Potential (electron-electron) energy contribution in DFT formalism

$U_{en}[n(\mathbf{r})\ ]$ Potential (electron-nucleus) energy contribution in DFT formalism

$E_{XC}[n(\mathbf{r})\ ]$ Exchange-correlation energy contribution in DFT formalism

λ Lagrange multiplier

ε_k Energy associated with a single-particle orbital ψ_k

Ψ_T Trial wave function

p_y Parameters in Ψ_T

Ψ_0 Ground state wave function

E_T Trial energy

$P(\mathbf{r})$ Probability sampled by the Metropolis Algorithm

E_L Local energy

σ^2 Variance

$\Phi^{(i)}$ i^{th} wave function during the linear method for optimization procedure

c_y Coefficients for the linear method

N_v Number of parameters in Ψ_T

H_{xy} Hamiltonian matrix element

S_{xy} Overlap matrix element

$J(r; \{p_y\})$ Jastrow factor

p_{wyz} Parameter in the three-body Jastrow factor

M_{ee} Polynomial order in the three-body Jastrow factor for electron-electron distance

M_{eI} Polynomial order in the three-body Jastrow factor for electron-ion distance

$\Psi_{SD}^{\uparrow}$ Slater Determinant with up-spin electrons

$\Psi_{SD}^{\downarrow}$ Slater Determinant with down-spin electrons

$\mathbf{R}_L$ Unit cell lattice vector

$\mathbf{G}$ Reciprocal lattice vector

Γ Central k point at reciprocal space

$\mathbf{R}_S$ Supercell lattice vector

θ Reciprocal lattice vector in the SC

Δ Displacement parameter in the Metropolis Algorithm

$E_{coh}(A_x B_y)$ Cohesive energy of the compound $A_x B_y$

$E_{form}(A_x B_y)$ Formation energy of the compound $A_x B_y$

a Lattice parameter. Fitting parameter for the specific heat

b Lattice parameter. Fitting parameter for the specific heat

c Lattice parameter

ΔE_T Decrease in the trial energy after the wave function optimization

ΔH_{form} Enthalpy of formation

C_P Specific heat

C_V^{deb} Specific heat in the Debye's model

Θ_D Debye's temperature

T Temperature

$D\left(\frac{\Theta_D}{T}\right)$ Debye's function

N_B Block size in the blocking averages procedure

N_{blocks} Number of blocks in the blocking averages procedure

Contents

Chapter 1

INTRODUCTION

At atomistic scale, nature is described by the equations of quantum mechanics. However, the analitical solution of the $3N$ dimensional problem, where N accounts to the number of particles in the system, remains unknown. Since the introduction of Schrödinger's equation, many approximations have been proposed to turn theoretical studies at atomic scale possible.

First principles, or *ab initio*, methods attempt to theoretically study a given system without considering empirical data. Nowadays, there is a huge variety of such methods, covering many levels of precision, which allows a deep understanding of simple molecules, systems of biological interest, nanoparticles, crystalline systems, among others. In addition, the computational study leads to high accuracy predictions, which might be usefull in predicting properties that cannot be measured yet, or present a difficulty in an experiment, such as a higher cost or toxicity.

Regarding atomistic solid state simulations, most of the computations are performed through Density Functional Theory (DFT), which is already an established theory. The use of the electronic density as main variable and the availability of several exchange-correlation functionals, that attempt to describe the electronic density of a given system, has turned possible considerable studies using DFT techniques. The computational cost associated to a DFT simulation allows its sucessful use in many fields, leading to several contributions in a diverse range of scientific questions. As examples, we can mention studies of surface reactions, nanotechnology, semiconductors and many others [1].

Additionally to DFT, Quantum Monte Carlo (QMC), which includes different techniques, being the most used the Variational Monte Carlo (VMC) and the Diffusion Monte Carlo (DMC), uses stochastic methods to solve the $3N$ dimension problem. Briefly speaking, Fermionic VMC calculations consists in including correlation terms in a Slater-Determinant to form a trial wave function, which is further optimized to get an upper-bound of the variational energy. DMC, on its turn, is a projective method that filters out the excited states from a description of the system so that the ground state properties can be readly investigated [2].

Recent developments in computer resources have turned feasible the use of VMC and DMC to simulate larger systems, such as solids and atoms with larger Z. A notable research topic covering QMC simulations consists in the use of these methods to calculate the cohesive energy of a solid. By comparing the obtained results with the experimental

data, one is able to estimate the QMC level of accuracy [3].

In contrast to DFT, DMC is able to deliver results with errors within 1 kcal·mol or, approximately, 0.04 eV, in respect to the thermochemical measure [4]. Such accuracy is commonly denoted as *chemical accuracy* and it is achievable by employing higher level *ab initio* methods. Pozzo and Alfè [5] studied the properties of MgH_2 by DMC and DFT. Their DMC results present excellent agreement with the experimental data, although the chemical accuracy was not achieved. On the other hand, the DFT results presented uncertainties and were strongly dependent upon the exchange-correlation functional employed.

However, it is worth mention that the techniques previously described, DFT, VMC and DMC, are not fully apart from each other. Since QMC presents a higher computational cost, trial wave functions used in the VMC procedure might be benefited by the use of results from previous DFT calculations. In addition, the DMC guide function is actually the VMC optimized wave function. Regarding these methods accuracy, DFT is the less precise, due to approximations in the exchange-correlation functional. On the other hand, QMC methods are exact, being VMC dependent upon the trial wave function used and DMC, on the nodal structure of the guiding function.

1.1   Zr-Fe Intermetallics

Zr-Fe alloys constitute an example of a largely DFT studied system. It includes many stable intermetallics. Their compositions range from alloys mostly formed by Fe, like Zr_6Fe_{23}, to the *Zr-rich* ones, such as Zr_3Fe [6, 7]. Zr intermetallics are commonly used at nuclear industry, as fuel claddings, in continuous contact with water.

Several studies have been done in order to acess Zr-Fe phase diagram and its thermodynamic data [8, 7, 9]. According to Jiang and co-authors [7], Zr_2Fe enthalpy of formation, i.e., the energy change in the reaction

$$2Zr + Fe \rightarrow Zr_2Fe, \tag{1.1}$$

for 298 K and obatined using thermodynamic data, is -20.440 kJ·mol^{-1}, which is equivalent to -4.8853 kcal·mol^{-1}. On the other hand, Colinet *et al.* [8] reports -20 kJ·mol^{-1}, or, approximately, -4.8 kcal·mol^{-1}. For Zr_3Fe, the enthalpy obtained by Jiang *et al.*, at 298 K, is -16.121 kJ·mol^{-1}, or -3.8530 kcal·mol^{-1}, whereas Colinet and co-authors obtained -16.5 kJ·mol^{-1}, or -3.94 kcal·mol^{-1}.

These intermetallics present high hydrogen absorption capability, this is a reaction of concern in industry [10]. Hydrogen has been pointed out as a renewable fuel in vehicles and its isotopes play a fundamental role as nuclear fusion fuels [11]. Nowadays, its storage presents a challenge, due to explosion risks in its gas phase [12, 13]. A suitable solution consists in employing a crystalline material, which could keep hydrogen atoms in its interstices that moreover would allow an easy gas removal [11, 13]. In order to do so, many compounds have been extensively studied and we highlight Mg and Zr metals. In the previously mentioned study by Pozzo *et al.*, the enthalpy of formation of the hydride MgH_2 is calculated through DMC. Regarding the use of Zr, several hydride phases have been observed [10]. However, FeH has not been experimentally observed yet [14]. In

addition, $ZrFe_2$ is a bad hydride former, it is used when hydrogenation is to be avoided [10]. However, Zr-rich intermetallics, such as Zr_2Fe and Zr_3Fe are good candidates for hydrogen storage [15]. This suggests that the amount of H stored might be tunned, according to the alloy composition.

Zr_2Fe is produced under the trade name of St 198 and its hydrogen absorption have been studied by several authors. Its complete hydrogenation forms the compound Zr_2FeH_5 and the reaction is described by the following equation,

$$Zr_2Fe + \frac{5}{2}H_2 \rightarrow Zr_2FeH_5. \tag{1.2}$$

Nobile and its co-workers [16] performed an experimental study in the deuterium absorpion of Zr_2Fe, leading to the non-stoichiometric hydride Zr_2FeD_x, where $0 < x < 3$. According to their results, the activation takes place at temperatures above 623.15 K, though higher temperatures might lead to undersirable reactions, such as decompositions in ZrD_2, $ZrFe_2$ and Zr_2Fe or ZrD_2 and Fe. The authors have also derived an absorption enthalpy of 101.8 kJ·mol D_2.

Regarding the intermetallic Zr_3Fe, it has been observed several hydrides phases, ranging from low to higher concentrations of H. Similarly to the Zr_2Fe, Zr_3Fe hydrides also have the tendency in decomposing in $ZrFe_2$ and ZrH_2 in higher temperatures. [17]. Due to this issue, the partial substitution of Zr in the hydride have been investigated in order to allow the use of Zr_3Fe in the hydrogen storage [18]. Zr_3Fe reaction with hydrogen occurs through

$$Zr_3Fe + \frac{7}{2}H_2 \rightarrow Zr_3FeH_7. \tag{1.3}$$

Zr-Fe hydrides have also been intensely investigated by *ab initio* calculations. Chattaraj *et al.* [19] used DFT calculations to model electronic and termodynamic properties of Zr_2Fe and Zr_2FeH_5. Parameters of their lattices presented a reasonable agreement with the experimental values. Relative energies show that Zr_2FeH_5 is more stable than its precursor Zr_2Fe. On the other hand, Matar *et al.* [14] used DFT to compare the stability in the series ZrH_2, Zr_2FeH_5, ZrH_2 and FeH (hypothetical). Their geometry optimizations were in agreement with those of Chattaraj *et al.* [19]. In addition, they observed how the stabilization is related to the amounts of iron and zirconium in the hydrides.

However, as previously stated, DFT is an approximate theory and its results might not present a desirable accuracy. It is worth mention that Ali and co-workers [15] have calculated cohesive and formation energies for Zr_2Fe and Zr_3Fe, for example, with results that present higher deviations in relation to the experimental values. To the best of our knowledge, it has not been published a study covering any intermetallic of Zr-Fe system, nor any of their hydrides, at a QMC theoretical level.

1.2 Objectives

In this work, the focus is in the comparision of DFT results, using the Perdew-Burke-Ernzerhof (PBE) exchange-correlation functional, and VMC results, regarding their final

accuracy. This is done by calculation the formation entalpies of Zr_2FeH_5 and Zr_3FeH_7, starting from their corresponding alloys, Zr_2Fe and Zr_3Fe, and the forming metals, Zr and Fe. Such calculations were performed using both methods. The trial wave functions we employ in the VMC simulations are of the Slater-Jastrow form, which is formed by single particle orbitals (obtained from the DFT calculations) and correlation terms.

Initially, DFT is used to achieve equilibrium parameters for both solid and isolated systems. At these optimized geometries, we obtain the desired energetics data at DFT level. The correlations terms considers one- and two-body terms in VMC calculations that are optimized to obtain an upper-bound of the energy. After that, cohesive energies and the variation of entalphy are calculated. The final results are compared with experimental and published data.

Chapter 2

PROBLEM STATEMENT

2.1 Many-Electrons Wave Functions

A M nuclei system, with a total electrons number equal to N is described, in atomic units, by the Hamiltonian

$$H = -\sum_{i=1}^{N} \frac{1}{2}\nabla_i^2 - \sum_{A=1}^{M} \frac{1}{2M_A}\nabla_A^2 - \sum_{i=1}^{N}\sum_{A=1}^{M} \frac{Z_A}{r_{iA}} + \sum_{i=1}^{N}\sum_{i<j}^{N} \frac{1}{r_{ij}} + \sum_{A=1}^{M}\sum_{B>A}^{M} \frac{Z_A Z_B}{R_{AB}}. \qquad (2.1)$$

In the previous equation, the fisrt two terms account for the kinetic energies of electrons and nuclei, respectively, followed by electron-nucleus attraction and, finally, electron-electron and nucleus-nucleus repulsions [20]. A complexity that arises in solving Schrödinger Equation for such system consist in repulsion terms, which correlates the probability of finding a given electron at a given position to the presence of other electron nearby. In addition, to correctly describe a fermionic system, the wave function must obey certain requirements, such as the spin dependence due to the exclusion principle. Lastly, the number of terms of the summations in Equation 2.1 must be reduced, otherwise its calculation will not be computational feasible.

In general, the nuclei motion is much slower, when compared to the electrons movement. This occur because the nuclear mass is much higher than that of an electron. Thus, it is reasonable to split Equation 2.1 into electronic,

$$H_{elec} = -\sum_{i=1}^{N} \frac{1}{2}\nabla_i^2 - \sum_{i=1}^{N}\sum_{A=1}^{M} \frac{Z_A}{r_{iA}} + \sum_{i=1}^{N}\sum_{j>i}^{N} \frac{1}{r_{ij}}, \qquad (2.2)$$

and nuclear,

$$H_{nucl} = -\sum_{A=1}^{M} \frac{1}{2M_A}\nabla_A^2 + \sum_{A=1}^{M}\sum_{B>A}^{M} \frac{Z_A Z_B}{R_{AB}}, \qquad (2.3)$$

Hamiltonians and then solve both terms separately [21]. Thus the wave function is written

as the following product,

$$\Phi\left(\{\mathbf{r}\}, \{\mathbf{R}\}\right) = \Psi(\{\mathbf{r}\}; \{\mathbf{R}\})\Theta\left(\{\mathbf{R}\}\right). \tag{2.4}$$

In which $\Theta\left(\{\mathbf{R}\}\right)$ stands for the nuclear wave function, whereas $\Psi(\{\mathbf{r}\}; \{\mathbf{R}\})$, also written in the simplified notation $\Psi(\{\mathbf{r}\})$, is the electronic one and over which H_{elec} solely operates, leading to the eigenvalue ε_{elec} [22]. $\Psi(\{\mathbf{r}\}; \{\mathbf{R}\})$ presents a parametric dependence upon the nuclei coordinates, due to the fact the electronic Hamiltonian includes the electron-nucleus attraction term. Within this assumption, it is possible to obtain two coupled equations, one for electronic motion and, the other, standing for the nuclei. The result obtained with the electronic equation is used in order to solve the nuclear one [22]. In order to do so, we write the Schrödinger equation for the wave function of Equation 2.4,

$$(H_{elec} + H_{nucl})\Psi\left(\{\mathbf{r}\}\right)\Theta\left(\{\mathbf{R}\}\right) = \varepsilon_{tot}\Psi\left(\{\mathbf{r}\}\right)\Theta\left(\{\mathbf{R}\}\right), \tag{2.5}$$

where ε_{tot} stands for the system's total energy. By multiplying on the left by $\Psi^*(\{\mathbf{r}\})$ and integrating over electrons coordinates,

$$\int d\mathbf{r}_1...d\mathbf{r}_N\Psi^*(\{\mathbf{r}\})(H_{elec}+H_{nucl})\Psi(\{\mathbf{r}\})\Theta\left(\{\mathbf{R}\}\right) = \int d\mathbf{r}_1...d\mathbf{r}_N\Psi^*(\{\mathbf{r}\})\varepsilon_{tot}\Psi(\{\mathbf{r}\})\Theta\left(\{\mathbf{R}\}\right),$$

and using the fact H_{elec} operates solely in $\Psi(\{\mathbf{r}\})$, returning ε_{elec},

$$\varepsilon_{elec}\Theta\left(\{\mathbf{R}\}\right) + \int d\mathbf{r}_1...d\mathbf{r}_N\Psi^*(\{\mathbf{r}\})H_{nucl}\Psi(\{\mathbf{r}\})\Theta\left(\{\mathbf{R}\}\right) = \varepsilon_{tot}\Theta\left(\{\mathbf{R}\}\right), \tag{2.6}$$

The term dependent in H_{nucl} of Equation 2.6 can be explicitly written as

$$\int d\mathbf{r}_1...d\mathbf{r}_N\Psi^*(\{\mathbf{r}\})H_{nucl}\Psi(\{\mathbf{r}\})\Theta\left(\{\mathbf{R}\}\right) = \int d\mathbf{r}_1...d\mathbf{r}_N\Psi^*(\{\mathbf{r}\})\sum_{A=1}^{M} -\frac{\nabla_A^2}{2M_A}\Psi(\{\mathbf{r}\})\Theta\left(\{\mathbf{R}\}\right)$$

$$+ \int d\mathbf{r}_1...d\mathbf{r}_N\Psi^*(\{\mathbf{r}\})\sum_{B>A}^{M} \frac{Z_A Z_B}{R_{AB}}\Psi(\{\mathbf{r}\})\Theta\left(\{\mathbf{R}\}\right), \tag{2.7}$$

by using the chain rule in the 1st term on r.h.s., we can write

$$\int d\mathbf{r}_1...d\mathbf{r}_N\Psi^*(\{\mathbf{r}\})\sum_{A=1}^{M} -\frac{\nabla_A^2}{2M_A}\Psi(\{\mathbf{r}\})\Theta\left(\{\mathbf{R}\}\right) = -\sum_{A=1}^{M} \frac{1}{2M_A}\int d\mathbf{r}_1...d\mathbf{r}_N\Psi^*(\{\mathbf{r}\})\times$$

$$\times\left[\nabla_A^2\Psi(\{\mathbf{r}\}) + 2\nabla_A\Psi(\{\mathbf{r}\})\nabla_A + \Psi(\{\mathbf{r}\})\nabla_A^2\right]\Theta(\{\mathbf{R}\}). \tag{2.8}$$

Finally,

$$\left\{ \varepsilon_{elec} - \sum_{A=1}^{M} \frac{1}{2M_A} \left[\int d\mathbf{r}_1 ... d\mathbf{r}_N \Psi^*(\{\mathbf{r}\}) \nabla_A^2 \Psi(\{\mathbf{r}\}) + 2 \left(\int d\mathbf{r}_1 ... d\mathbf{r}_N \Psi^*(\{\mathbf{r}\}) \nabla_A \Psi(\{\mathbf{r}\}) \right) \nabla_A \right. \right.$$

$$\left. \left. + \nabla_A^2 \right] + \sum_{B>A}^{M} \frac{Z_A Z_B}{R_{AB}} \right\} \Theta(\{\mathbf{R}\}) = \varepsilon_{tot} \Theta(\{\mathbf{R}\}). \tag{2.9}$$

At the previous equation, the 2nd and 3rd terms of the l.h.s. are called 1st and 2nd order non-adiabatic coupling terms, respectivelly. If such terms were neglected, which is possible due to the fact the electrons move rapidly, adiabatically, in response to the slow change of the nuclei positions [22], we have the Born-Oppenheimer Approximation (BOA). Equation 2.9 is then reduced to

$$\left(\varepsilon_{elec} - \sum_{A=1}^{M} \frac{\nabla_A^2}{2M_A} + \sum_{B>A}^{M} \frac{Z_A Z_B}{R_{AB}} \right) \Theta(\{\mathbf{R}\}) = \varepsilon_{tot} \Theta(\{\mathbf{R}\}). \tag{2.10}$$

In the Equation 2.10, the term ε_{elec} can be interpreted as a potential term in the nuclear Schrödinger equation. Thus, both nuclear and electronic equations could be solved separately [23]. Moreover, the solution of the electronic equation constitutes the so-called Potential Energy Surfaces (PES), in which the nuclear motion occur. As a consequence, it turns possible the investigation of equilibrium and transition-state geometries [21, 22].

Turning now our attention into the electronic Schrödinger equation, it is important to remind the two properties which must be considered: the exclusion principle and electronic correlations. An initial approach to solve the electronic Hamiltonian is to assume a non-interacting system, thus the last term in Equation 2.2 is neglected and $\Psi(\{\mathbf{r}\})$ might be expressed as

$$\Psi(\{\mathbf{r}\}) = \prod_{i}^{N} \psi_i(\mathbf{r}_i), \tag{2.11}$$

i.e. a product of single-particle wave functions, $\psi_i(\mathbf{r}_i)$. This approximation is refered as the Hartree product and is commonly invoked in several *ab initio* methods, including the DFT.

According to the Pauli exclusion principle, $\Psi(\{\mathbf{r}\})$ needs to be spin dependent and anti-symetric with respect to interchange of coordinates (including spin) of two electrons. The spin is included by employing $\alpha(\sigma)$ and $\beta(\sigma)$ functions, in which σ is a spin variable [20]. These functions are defined to form a complete and orthonormal set in the spin space of spin 1/2 particles. Therefore, from any single electron spatial wave function, $\psi_k(\mathbf{r}_i)$, one can write the corresponding spin orbitals, $\psi_k(\mathbf{r}_i,\sigma)$, or merely $\psi_k(\mathbf{x}_i)$, where $\mathbf{x}$ accounts for both spatial coordinates and spin [20]. For an electron i with an up-spin, we write

$$\psi_i(\mathbf{r}_i)\alpha(\sigma) = \psi_i(\mathbf{x}_i) \tag{2.12}$$

and, for a j down-spin electron,

$$\psi_j(\mathbf{r}_j)\beta(\sigma) = \psi_j(\mathbf{x}_j). \tag{2.13}$$

After including spin variables and expressing $\Psi(\{\mathbf{x}\})$ as a Hartree product, it still lacks antisymmetry and does not include electrons indistinguishability. Nonetheless, it is possible to generate an antisymmetric wave function by a linear combination of Hartree products. By arranging $\{\psi(\mathbf{x})\}$ in a determinant, we achieve a global antysimetric wave function with indistinguishable electrons [20]

$$\Psi(\{\mathbf{x}\}) = \frac{1}{\sqrt{N!}} \begin{vmatrix} \psi_1(\mathbf{x}_1) & \psi_2(\mathbf{x}_1) & ... & \psi_N(\mathbf{x}_1) \\ \psi_1(\mathbf{x}_2) & \psi_2(\mathbf{x}_2) & ... & \psi_N(\mathbf{x}_2) \\ . & . & & . \\ . & . & & . \\ . & . & & . \\ \psi_1(\mathbf{x}_N) & \psi_2(\mathbf{x}_N) & ... & \psi_N(\mathbf{x}_N) \end{vmatrix}. \tag{2.14}$$

where $\frac{1}{\sqrt{N!}}$ is a normalization factor. This determinant is called Slater-Determinant and assures an antisymmetric global wave function [20]. Finally, it remains to include electron-electron correlations. In the DFT method it is done through an effective potential, whereas, in QMC methods, correlation terms are added in trial wave functions.

2.2   Pseudopotentials

Pseudopotentials are effective potentials that describe the nucleus and core electrons, in a simplified manner. Such replacement is possible because valence electrons do not feel the entire nuclear potential, it is shielded by core electrons [24].

The main reason in avoiding an all-electron calculation lies at the computational cost. It might be extremely considerable in all electrons calculations of large systems, such as transition metals [24]. In addition, if Z is increased, larger and specialized basis sets are required or, if a plane-waves basis set is used, the number of functions needed for convergence grows in a manner that prevents such calculations [25].

Another reason for using pseudopotentials is related to the nuclear potential divergence at the core region (Figure 2.1(a)). Inside this region, electronic wave functions present a rapid oscillation, as can be seen in Figure 2.1(b). These factors contribute to the increase of the computational cost [26].

In order to derive a pseudopotential, we write a valence orbital $|\psi_v\rangle$, emphasizing its orthogonality to the core states $\{|\psi_c\rangle\}$ [27, 28]:

$$|\psi_v\rangle = |\varphi_v\rangle - \sum_c |\psi_c\rangle\langle\psi_c|\varphi_v\rangle, \tag{2.15}$$

where $|\varphi_v\rangle$ is called pseudo wave function that turns to be a smooth function, whereas the 2nd term on r.h.s. arises from orthogonality requirements: the projector $|\psi_c\rangle\langle\psi_c|$ selects all components of $|\varphi_v\rangle$ which are parallel to $|\psi_c\rangle$, thus by employing such term with the negative sign, we assure the valence orbital $|\psi_v\rangle$, written in the basis of $|\varphi_v\rangle$
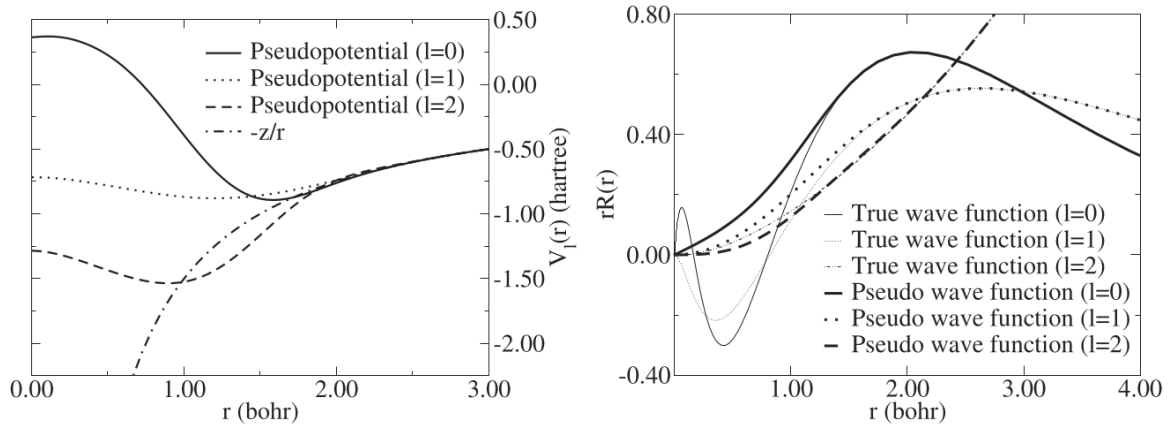
(a) Original potential and pseudopotential plots as a function of the radial distance [27].

(b) Original and pseudo wave functions plots as a function of the radial distance [27].

remain orthogonal to $\{|\psi_c\rangle\}$. By applying the Hamiltonian of Equation 2.2 (that now on will be denoted only by H) in $|\psi_v\rangle$,

$$H|\psi_v\rangle = E_v|\psi_v\rangle, \tag{2.16}$$

one obtains an eigenvalue equation for $|\varphi_v\rangle$:

$$H|\varphi_v\rangle = E_v|\varphi_v\rangle + \sum_c \left(E_c - E_v\right)|\psi_c\rangle\langle\psi_c|\varphi_v\rangle, \tag{2.17}$$

where E_v and E_c are the energy eigenvalues for $|\psi_v\rangle$ and $|\psi_c\rangle$, respectively. By rearranging these terms, we get

$$\left[H - \sum_c \left(E_c - E_v\right)|\psi_c\rangle\langle\psi_c|\right]|\varphi_v\rangle = E_v|\varphi_v\rangle, \tag{2.18}$$

where we can identify the pseudopotential [28]

$$V^{PP}(E) = -\sum_c \left(E_c - E_v\right)|\psi_c\rangle\langle\psi_c|, \tag{2.19}$$

which is a repulsive potential and stands for an attenuation of the potential felt by the valence electrons. It is known that this term dominates at the nucleus vicinity, thus the resulting potential is softned. Outside the core region, the repulsive potential term vanishes, hence the system is described by the Hamiltonian H of Equation 2.2 and its associated wave function [27].

We define the core region by a radius, r_c. Beyond this distance, the electronic wave function is identical to the pseudo wave function. At r_c, these functions and their derivatives should be equal [27, 29]. As much as the pseudopotential becomes closer to the original potential for small values of r_c, a larger basis set is needed in the calculations [24].

The pseudopotential we use in this work presents a dependence in the angular momentum. They are known as non-local pseudopotentials [24, 27]. If we could neglect this

dependence, we would have a local pseudopotential, which is simpler and depends only upon radial distance.

Another common classification of pseudopotentials is related to the pseudo wave functions norms inside the core region. When pseudo and original wave functions norms are equal, the pseudopotential is called Norm Conserving Pseudopotential (NCPP)[27]. Although, NCPPs present high accuracy and flexibility for use in several chemical environments, the norm conservation requirement might give rise to hard potentials. This means that the associated wave functions present higher curvatures and, consequently, require larger basis sets in order to exhibit the desired accuracy [24, 29]. Due to such increase at computational cost, norm-conservation constrain was removed for some pseudopotentials, propting the creation of Ultrasoft Pseudopotentials (USPP). For this kind of potential, there is no constraint for norm-conservation and core radius is allowed to increase without loss of accuracy [30]. Furthermore, USPPs demands smaller basis sets, when compared to NCPPs [24].

Finally, for a right choice of the pseudopotential in a given calculation, one must take into account its transferability. It stands for the capacity of correclty reproducing an all electron calculation at different chemical environments, such as other oxidation states. Testing the pseudopotential according to the desired prediction is mandatory [24].

2.2.1 Norm-Conserving Pseudopotentials

As mentioned before, NCPPs require the pseudo-wave functions to remain normalized inside the core radius. An example of NCPP is the Rappe-Rabe-Kaxiras-Joannopoulos (RRKJ) pseudopotential [25]. For the RRKJ pseudopotential, pseudo wave functions are choosen in order to use a smaller basis set, though still large comparing with a USPP. Thus, this pseudopotential is commonly refered as optimized pseudopotential [25].

Pseudo wave functions are composed by a sum of two functions: $F_l(r)$ and a correction function $C_l(r)$. The subscript l is included in order to emphasize the dependence upon the angular momentum. $F_l(r)$ optimizes the pseudo wave function kinetic energy and $C_l(r)$, the energy convergence of the original atomic wave function [25]. Therefore, φ_v is written as

$$\varphi_v(r) = F_l(r) + C_l(r) \qquad r \leq r_c, \tag{2.20}$$

where, r_c is the core radius. $F_l(r)$ is written as a sum of four Bessel functions:

$$F_l(r) = \sum_{i=1}^{4} a_i j_l(r, \mathbf{k}_i), \tag{2.21}$$

four functions are needed to assure both its normalization and continuity of $F_l(r)$ and its first derivative. On the other hand, their wave vectors $\mathbf{k}_i$ are choosen to obey the following relation:

$$\frac{j_l'(r, \mathbf{k}_i)}{j_l(r, \mathbf{k}_i)} = \frac{\psi_l'(r_c)}{\psi_l(r_c)}, \tag{2.22}$$

where $j'_l(r, \mathbf{k}_i)$ and $\psi'_l(r_c)$ are Bessel functions and the original wave functions, i.e. the functions related to the Hamiltonian of Equation 2.2, derivatives with respect to r, respectively. Coefficients $\{a_i\}$ are choosen in order to obey normalization and continuity requirements.

Regarding the correction function, $C_l(r)$, it is again expanded as a combination of Bessel functions

$$C_l(r) = \sum_{i=1}^{N} b_i j_l(r, \mathbf{k}_i). \tag{2.23}$$

The wave vectors $\mathbf{k}_i$ are defined so that the Bessel functions have a node at $r = r_c$,

$$j_l(r_c, \mathbf{k}_i) = 0, \tag{2.24}$$

and the coefficients b_i are choosen to minimize the kinetic energy beyond values of $\mathbf{k}_c$, which is called cutoff wave vector.

Once the pseudo wave functions are defined, the pseudopotential for $r \leq r_c$ is found by writing the Schrödinger Equation for $r \leq r_c$,

$$\left[-\frac{1}{2} \frac{d^2}{dr^2} + \frac{l(l+1)}{2r^2} + V^{PP}(r) \right] \varphi_l(r) = E_l \varphi_l(r), \tag{2.25}$$

and isolating the $V^{PP}(r)$ term,

$$V^{PP}(r)\varphi_l(r) = \left[E_l - \frac{l(l+1)}{2r^2} \right] \varphi_l(r) + \frac{1}{2} \frac{d^2}{dr^2} \varphi_l(r) \tag{2.26}$$

$$V^{PP}(r) = E_l - \frac{l(l+1)}{2r^2} + \frac{1}{2\varphi(r)} \frac{d^2}{dr^2} \varphi_l(r) - \frac{l(l+1)}{2r^2}. \tag{2.27}$$

In the RRKJ pseudopotential, electronic correlations are included using the Density Functional Theory formalism, through the Local Density Approximation functional.

For $r > r_c$, the potential returns to its original form in the last two terms of Equation 2.2, i.e., the nuclear and electron-electron contributions. Similarly, the wave function is expressed as $\psi_l(\mathrm{r})$.

Chapter 3

DENSITY FUNCTIONAL THEORY

In the Density Functional Theory (DFT) formalism, done under BOA, the electronic density, denoted by $n(\mathbf{r})$, is used as main variable, instead of each electron coordinate. DFT is reasoned in the Hohenberg-Kohn theorems [1]:

- The density of a system determines all their ground-state properties, i.e., the energy and related observables are functionals of $n(\mathbf{r})$. This density is defined by

$$n(\mathbf{r}) = \sum_i |\psi_i(\mathbf{r})|^2, \tag{3.1}$$

with

$$\int d\mathbf{r}\, n(\mathbf{r}) = N. \tag{3.2}$$

- The Variational Principle guaranties that the ground-state energy might be obtained once the ground state density $n_0(\mathbf{r})$ is known

$$E[n_0(\mathbf{r})] < E[n(\mathbf{r})]. \tag{3.3}$$

An eigenvalue equation for $E[n(\mathbf{r})]$ is derived by using a hypothetical non-interacting system, known as a Hatree system, in which the electronic density should be equal to the real system density. The total energy is partioned into kinetic, $T[n(\mathbf{r})]$, potential (electron-electron repulsion, $U_{ee}[n(\mathbf{r})]$, and electron-nucleus attraction, $U_{en}[n(\mathbf{r})]$) and exchange-correlation, $E_{XC}[n(\mathbf{r})]$, which accounts for the differences between the Hartree and real systems [21],

$$E[n(\mathbf{r})] = T[n(\mathbf{r})] + U_{en}[n(\mathbf{r})] + U_{ee}[n(\mathbf{r})] + E_{XC}[n(\mathbf{r})]. \tag{3.4}$$

Using the Hartree product of single particle orbitals (Equation 2.11), we write expectation values of the kinetic and potential energies [21],

$$T[n(\mathbf{r})] = \sum_i \int d\mathbf{r}\, \psi_i^*(\mathbf{r}) \left(-\frac{1}{2}\nabla_i^2\right) \psi_i(\mathbf{r}), \tag{3.5}$$

$$U_{en}[n(\mathbf{r})] = \sum_i \int d\mathbf{r}\psi_i^*(\mathbf{r}) \left(\sum_{A=1}^{M} \frac{Z_A}{|\mathbf{r} - \mathbf{r}_A|} \right) \psi_i(\mathbf{r}) = \int d\mathbf{r} \sum_i |\psi_i(\mathbf{r})|^2 \left(\sum_{A=1}^{M} -\frac{Z_A}{|\mathbf{r} - \mathbf{r}_A|} \right)$$

$$= \int d\mathbf{r} \left(\sum_{A=1}^{M} -\frac{Z_A}{|\mathbf{r} - \mathbf{r}_A|} \right) n(\mathbf{r}) \tag{3.6}$$

and

$$U_{ee}[n(\mathbf{r})] = \frac{1}{2} \sum_{i,j \neq i} \int d\mathbf{r}d\mathbf{r}' \Psi_i^*(\mathbf{r})|\Psi_j(\mathbf{r}')|^2 \frac{1}{|\mathbf{r} - \mathbf{r}'|} \Psi_i(\mathbf{r})$$

$$= \frac{1}{2} \sum_{j \neq i} \int d\mathbf{r}d\mathbf{r}' \frac{n(\mathbf{r})|\Psi_j(\mathbf{r}')|^2}{|\mathbf{r} - \mathbf{r}'|}. \tag{3.7}$$

Equation 3.7, accounts for the repulsion between two electrons, localized on orbitals ψ_i and ψ_j, at positions $\mathbf{r}$ and $\mathbf{r}$', respectively. The factor $\frac{1}{2}$ avoids double counting due to no restriction $i < j$ on summations [21]. By substituting Equations 3.5-3.7 into Equation 3.4, we have

$$E[n(\mathbf{r})] = \sum_i^N \int d\mathbf{r}\psi_i^*(\mathbf{r}) \left(-\frac{1}{2}\nabla_i^2 \right) \psi_i(\mathbf{r}) + \int d\mathbf{r} \left(\sum_{A=1}^{M} -\frac{Z_A}{|\mathbf{r} - \mathbf{r}_A|} \right) n(\mathbf{r}) +$$

$$+\frac{1}{2} \sum_{j \neq i} \int d\mathbf{r}d\mathbf{r}' \frac{n(\mathbf{r})|\Psi_j(\mathbf{r}')|^2}{|\mathbf{r} - \mathbf{r}'|} + E_{XC}[n(\mathbf{r})]. \tag{3.8}$$

In the following step, we invoke the variational principle in order to minimize Equation 3.8 with respect to each orbital $\psi_i^*(\mathbf{r})$, since we intend to derive an expression for $\psi(\mathbf{r})$, not for $\psi^*(\mathbf{r})$. Such minimization is performed with the constraint that the single-particle orbitals remain orthonormal.

In order to do so, Langrange multipliers are employed:

$$\frac{\delta}{\delta\psi_k^*(\mathbf{r})} \left\{ E[n(\mathbf{r})] - \sum_{i,j} \lambda_{ij} \left[\int d\mathbf{r}_i d\mathbf{r}_j \psi_i^*(\mathbf{r}_i)\psi_j(\mathbf{r}_j) - \delta_{ij} \right] \right\} = 0$$

$$\frac{\delta E[n(\mathbf{r})]}{\delta\psi_k^*(\mathbf{r})} = \frac{\delta}{\delta\psi_k^*(\mathbf{r})} \left\{ \sum_{i,j} \lambda_{ij} \left[\int d\mathbf{r}_i d\mathbf{r}_j \psi_i^*(\mathbf{r}_i)\psi_j(\mathbf{r}_j) - \delta_{ij} \right] \right\}. \tag{3.9}$$

The integral on r.h.s. of Equation 3.9 will be non-zero only for $i = j$, whereas functional derivative accounts for $i = k$. Thus,

$$\frac{\delta E[n(\mathbf{r})]}{\delta\psi_k^*(\mathbf{r})} = \lambda_{kk}\psi_k(\mathbf{r}). \tag{3.10}$$

Now, taking the functional derivative, with respect to $\psi_k^*(\mathbf{r})$, of $E[n(\mathbf{r})]$ in Equation 3.4,

we have

$$\frac{\delta E[n(\mathbf{r})]}{\delta \psi_k^*(\mathbf{r})} = \frac{\delta}{\delta \psi_k^*(\mathbf{r})} \{T[n(\mathbf{r})] + U_{en}[n(\mathbf{r})] + U_{ee}[n(\mathbf{r})] + E_{XC}[n(\mathbf{r})]\}. \tag{3.11}$$

The functional derivative of $T[n(\mathbf{r})]$ gives

$$\frac{\delta T[n(\mathbf{r})]}{\delta \psi_k^*(\mathbf{r})} = \frac{\delta}{\delta \psi_k^*(\mathbf{r})} \left[\sum_i \int d\mathbf{r} \psi_i^*(\mathbf{r}) \left(-\frac{1}{2} \nabla_i^2 \right) \psi_i(\mathbf{r}) \right]$$

$$= -\frac{1}{2} \nabla_k^2 \psi_k(\mathbf{r}). \tag{3.12}$$

For $U_{en}[n(\mathbf{r})]$ and $U_{ee}[n(\mathbf{r})]$, we have:

$$\frac{\delta U_{en}[n(\mathbf{r})]}{\delta \psi_k^*(\mathbf{r})} = \frac{\delta U_{en}[n(\mathbf{r})]}{\delta n(\mathbf{r})} \frac{\delta n(\mathbf{r})}{\delta \psi_k^*(\mathbf{r})}$$

$$= \frac{\delta}{\delta n(\mathbf{r})} \left[\int d\mathbf{r} \left(\sum_{A=1}^{M} -\frac{Z_A}{|\mathbf{r} - \mathbf{r}_A|} \right) n(\mathbf{r}) \right] \frac{\delta}{\delta \psi_k^*(\mathbf{r})} \left[\sum_i |\psi_i(\mathbf{r})|^2 \right]$$

$$= -\left(\sum_{A=1}^{M} \frac{Z_A}{|\mathbf{r} - \mathbf{r}_A|} \right) \psi_k(\mathbf{r}) \tag{3.13}$$

and

$$\frac{\delta U_{ee}[n(\mathbf{r})]}{\delta \psi_k^*(\mathbf{r})} = \frac{\delta}{\delta n(\mathbf{r})} \left[\frac{1}{2} \sum_{j \neq i} \int d\mathbf{r} d\mathbf{r}' \frac{n(\mathbf{r})|\psi_j(\mathbf{r}')|^2}{|\mathbf{r} - \mathbf{r}'|} \right] \frac{\delta n(\mathbf{r})}{\delta \psi_k^*(\mathbf{r})}$$

$$= \frac{1}{2} \left[\sum_{j \neq i} \int d\mathbf{r}' \frac{|\psi_j(\mathbf{r}')|^2}{|\mathbf{r} - \mathbf{r}'|} \right] \psi_k(\mathbf{r}). \tag{3.14}$$

In order to simplify the following steps, the restrictions $j \neq i$ and the factor $\frac{1}{2}$ on summation at Equation 3.14 will be removed. This leads to a *self-interaction* error, which must be corrected in E_{XC} term. Thus, Equation 3.14 is reduced to

$$\frac{\delta U_{ee}[n(\mathbf{r})]}{\delta \psi_k^*(\mathbf{r})} = \int d\mathbf{r}' \frac{n(\mathbf{r}')}{|\mathbf{r} - \mathbf{r}'|} \psi_k(\mathbf{r}). \tag{3.15}$$

The exchange-correlation functional E_{XC} and the exchange-correlation potential V_{XC} are related by the equation

$$\frac{\delta E_{XC}[n(\mathbf{r})]}{\delta n(\mathbf{r})} = V_{XC}(r), \tag{3.16}$$

which leads to:

$$\frac{\delta E_{XC}[n(\mathbf{r})]}{\delta \psi_k^*(\mathbf{r})} = V_{XC}(r) \psi_k(\mathbf{r}) \tag{3.17}$$

Finally, we have the Kohn-Sham equation,

$$\left[-\frac{1}{2}\nabla_k^2 - \left(\sum_{A=1}^{M}\frac{Z_A}{|\mathbf{r}-\mathbf{r}_A|}\right) + \int d\mathbf{r}'\frac{n(\mathbf{r}')}{|\mathbf{r}-\mathbf{r}'|} + V_{XC}(r)\right]\psi_k(\mathbf{r}) = \lambda_{kk}\psi_k(\mathbf{r}), \qquad (3.18)$$

where the Lagrange multiplier λ_{kk} is identified as the $\psi_k(\mathbf{r})$ energy,

$$\lambda_{kk}\psi_k(\mathbf{r}) = \varepsilon_k\psi_k(\mathbf{r}). \qquad (3.19)$$

It is important to remind that wave functions we used are auxiliary Hartree single electron wave functions, for an hipothetical system.

In order to obtain an expression for the total energy, we multiply Equation 3.18 by $\sum_k \psi_k^*(\mathbf{r})$ on the left and integrate,

$$\sum_k \int d\mathbf{r}\psi_k^*(\mathbf{r}) \left[-\frac{1}{2}\nabla_k^2 - \left(\sum_{A=1}^{M}\frac{Z_A}{|\mathbf{r}-\mathbf{r}_A|}\right) + \int d\mathbf{r}'\frac{n(\mathbf{r}')}{|\mathbf{r}-\mathbf{r}'|} + V_{XC}(r)\right]\psi_k(\mathbf{r}) =$$

$$= \sum_k \int d\mathbf{r}\psi_k^*(\mathbf{r})\varepsilon_k\psi_k(\mathbf{r}). \qquad (3.20)$$

The first term is the kinetic energy term, Equation 3.5. Then, by taking into account the orthonormality of ψ_k, Equation 3.20 can be written as

$$T[n(\mathbf{r})] + \sum_k \int d\mathbf{r}\psi_k^*(\mathbf{r}) \left[\left(\sum_{A=1}^{M}\frac{-Z_A}{|\mathbf{r}-\mathbf{r}_A|}\right) + \int d\mathbf{r}'\frac{n(\mathbf{r}')}{|\mathbf{r}-\mathbf{r}'|} + V_{XC}(r)\right]\psi_k(\mathbf{r}) =$$

$$= \sum_k \varepsilon_k. \qquad (3.21)$$

Now, by substituting $T[n(\mathbf{r})]$ from Equation 3.4, we have

$$E[n(\mathbf{r})] = U_{en}[n(\mathbf{r})] + U_{ee}[n(\mathbf{r})] + E_{XC}[n(\mathbf{r})] + \sum_k \varepsilon_k +$$

$$-\sum_k \left[\int d\mathbf{r}\psi_k^*(\mathbf{r}) \left(\sum_{A=1}^{M}\frac{-Z_A}{|\mathbf{r}-\mathbf{r}_A|}\right)\psi_k(\mathbf{r}) + \int d\mathbf{r}d\mathbf{r}'\psi_k^*\frac{n(\mathbf{r}')}{|\mathbf{r}-\mathbf{r}'|}\psi_k(\mathbf{r})\right] +$$

$$-\sum_k \int d\mathbf{r}\psi_k^* V_{XC}(r)\psi_k(\mathbf{r}). \qquad (3.22)$$

By using Equation 3.1, the above equation becomes

$$E[n(\mathbf{r})] = U_{en}[n(\mathbf{r})] + U_{ee}[n(\mathbf{r})] + E_{XC}[n(\mathbf{r})] + \sum_k \varepsilon_k +$$

$$-\int d\mathbf{r} \left(\sum_{A=1}^{M} \frac{-Z_A}{|\mathbf{r}-\mathbf{r}_A|} \right) n(\mathbf{r}) - \int d\mathbf{r}d\mathbf{r}' \frac{n(\mathbf{r})n(\mathbf{r}')}{|\mathbf{r}-\mathbf{r}'|} - \int d\mathbf{r} V_{XC}(r) n(\mathbf{r}). \tag{3.23}$$

The substitution of Equations 3.6 and 3.7 gives the energy as

$$E[n(\mathbf{r})] = \sum_k \varepsilon_k - \frac{1}{2} \int d\mathbf{r}d\mathbf{r}' \frac{n(\mathbf{r})n(\mathbf{r}')}{|\mathbf{r}-\mathbf{r}'|} + E_{XC}[n(\mathbf{r})] - \int d\mathbf{r} V_{XC} n(\mathbf{r}). \tag{3.24}$$

As long V_{XC} is exact, $E[n(\mathbf{r})]$ is also exact, despite the use of auxilliary wave functions. Thus, the main concern about DFT is to obtain a functional which depends upon electronic density and that is able to correctly decribe all kinds of systems: atoms, molecules and solids [21]. Many functionals have been developed for such purpose, each one of them presenting its own description of the electronic density. As examples, we can mention the Local Density Approximation (LDA) and the Generalized Density Approximation (GGA), a family of functionals that include derivatives of the electronic density [21].

3.1 Local Density Approximation

The Local Density Approximation (LDA) is the first approach to obtain V_{XC} and, as used in RRKJ pseudopotential, it considers $n(\mathbf{r})$ as a locally uniform density at a $d\mathbf{r}$ region of the space, similar to an uniform electron gas. Thus, its exact energy per electron can be divided into exchange,

$$\varepsilon_X = -\frac{3}{4} \left(\frac{3}{\pi} \right)^{\frac{1}{3}} n^{\frac{1}{3}}, \tag{3.25}$$

and correlation terms [21],

$$\varepsilon_C = \begin{cases} A \ln r_S + B + C r_S \ln r_S + D r_S & r_S \leq 1 \\ \frac{\gamma}{1+\beta_1\sqrt{r_S}+\beta_2 r_S} & r_S > 1, \end{cases}$$

where r_S measures a certain cut-off distance for the Coulomb interaction range:

$$r_S = \left(\frac{3}{4\pi n} \right)^{\frac{1}{3}}. \tag{3.27}$$

E_{XC} in the LDA is given by

$$E_{XC}^{LDA}[n(\mathbf{r})] = \int d\mathbf{r} \varepsilon_{XC}^{gas}(\mathbf{r}) n(\mathbf{r}). \tag{3.28}$$

Although the exact form for E_{XC} in the LDA formalism can be derived, it is not a good approximation, since in most of systems in nature, the electronic density is not uniform [1]. As mentioned, the LDA will not yield good results in general. It is most suitable for pure solids, such as alcaline metals, where electronic density remains nearly constant.

3.2 Generalized Gradient Approximation

As the LDA is not able to adequately describe the electronic density of several systems, it is natural to propose more accurate functionals, which do not depend solely upon the density local value. Thus, many functionals include informations related to the density gradient. They are commonly refered as the Generalized Gradient Approximation (GGA) [21].

In general, GGA functionals add a correction term, which is dependent upon the reduced gradient, in the LDA E_{XC} [21],

$$\varepsilon_{XC}^{GGA} = \varepsilon_{XC}^{LDA} + \Delta\varepsilon_{XC}\left[\frac{\nabla n(\mathbf{r})}{n(\mathbf{r})^{4/3}}\right]. \qquad (3.29)$$

Contrary to the LDA, the GGA consists in a familly of functionals, in which some of them include empirical parameters in order to describe $n(\mathbf{r})$ [21]. In comparison with the LDA, the GGA functionals tend to improve results, such as atomization energies, energy barriers and structural energy differences [31].

An example of a GGA functional is the one proposed by Perdew, Burke and Ernzerhof (PBE), which does not use empirical parameters, but rather fundamental constants [31]. This is the functional that gave our best results.

Chapter 4

VARIATIONAL MONTE CARLO

Quantum Monte Carlo (QMC) techniques consist in methods that can be used to solve Schrödinger equation for many electron systems. When compared to other atomistic simulations, such as the DFT, Quantum Monte Carlo methods are able to deliver a higher precision in the results. They present a favorable scalling of $N^{2\sim 3}$, where N accounts for electrons number. In addition, the stochastic procedure is well suited for parallelization. Among the subdivisions of QMC, the most used are the Variational Monte Carlo (VMC) and the Difusion Monte Carlo (DMC) [32].

The VMC method consist in evaluating an integral by sampling a probability distribution. The estimation of the variational energy is usually done by the Metropolis algorithm, through successive samplings of the probability distribution. On the limit of infinite samplings, the average value converges to the exact one [33].

To begin this procedure, a trial wave function Ψ_T is proposed in order to describe the system under study. Such function depends upon a set of parameters $\{p_y\}$, which are chosen in order to yield the lowest trial energy (E_T), i.e. the energy associated with Ψ_T. Such energy is an upper bound to the ground state energy (E_0), according to the Variational Principle,

$$E_0 = \frac{\langle \Psi_0 | H | \Psi_0 \rangle}{\langle \Psi_0 | \Psi_0 \rangle} \leq \frac{\langle \Psi_T | H | \Psi_T \rangle}{\langle \Psi_T | \Psi_T \rangle} = E_T. \tag{4.1}$$

In the coordinates representation is useful to write Equation 4.1 as

$$\frac{\int d\mathbf{r} \frac{\Psi_T \Psi_T^* H \Psi_T}{\Psi_T}}{\int d\mathbf{r} \mid \Psi_T \mid^2} = E_T. \tag{4.2}$$

We can define a local energy as

$$E_L = \frac{H \Psi_T}{\Psi_T}, \tag{4.3}$$

and the probability,

$$P(\mathbf{r}) = \frac{\mid \Psi_T \mid^2}{\int d\mathbf{r} \mid \Psi_T \mid^2}, \tag{4.4}$$

which can be sampled through the Metropolis Algorithm and allows us to rewrite Equation 4.1 as

$$E_T = \int d\mathbf{r} P(\mathbf{r}) E_L. \tag{4.5}$$

In the limit of $N \to \infty$ samplings, the Monte Carlo method gives E_T. For N finite and large enough, it might be approximated as [34]

$$E_T \simeq \frac{1}{N} \sum_i^N E_L(\mathbf{r}_i). \tag{4.6}$$

Finally, it is important to compute the variance of E_T,

$$\sigma^2 = \frac{1}{N-1} \sum_i^N \left(E_L(\mathbf{r}_i) - E_T \right)^2. \tag{4.7}$$

The wave function optimization aims to obtain the optimum set of the $\{p_y\}$ which results in the lowest E_T. Another procedure is to minimize σ^2, due to the fact the ground-state is an eigenvalue of H [35, 34]. Furthermore, it is possible to define a *cost function*, that might be a linear combination of energy and variance, and minimize it [3]. A commonly used procedure for wave functions minimization is the Linear Method, which is employed in ready-to-use codes.

4.1   Linear Method for Wave function Optimization

In the linear method [36, 37], the wave function and its derivatives, with respect to each parameter p_y, are used to form a wave function with a new set of parameters,

$$|\Phi^{(1)}\rangle = \sum_{y=0}^{N_v} c_y |\Psi^y\rangle, \tag{4.8}$$

where N_v accounts for number of parameters to be optimized and $|\Psi^y\rangle$ is Ψ_T derivative with respect to the yth parameter,

$$|\Psi^y\rangle = \frac{\partial}{\partial p_y} |\Psi_T\rangle, \qquad \text{for } y \neq 0 \tag{4.9}$$

whereas

$$|\Psi^0\rangle = |\Psi_T\rangle. \tag{4.10}$$

The energy expectation value of $|\Phi^{(1)}\rangle$ is given by

$$E = \frac{\langle \Phi^{(1)}|H|\Phi^{(1)}\rangle}{\langle \Phi^{(1)}|\Phi^{(1)}\rangle} = \frac{\left(\sum_{y=0}^{N_v} \langle \Psi^y|c_y \right) H \left(\sum_{x=0}^{N_v} c_x |\Psi^x\rangle \right)}{\left(\sum_{y=0}^{N_v} \langle \Psi^y|c_y \right) \left(\sum_{x=0}^{N_v} c_x |\Psi^x\rangle \right)}. \tag{4.11}$$

Here, we introduce the notation for the matrix elements H_{xy} and S_{xy},

$$H_{xy} = \langle \Psi^y | H | \Psi^x \rangle \tag{4.12}$$

and

$$S_{xy} = \langle \Psi^y | \Psi^x \rangle. \tag{4.13}$$

Therefore, Equation 4.11 is rewritten as

$$E = \frac{\sum_{x,y}^{N_v} c_x c_y H_{xy}}{\sum_{x,y}^{N_v} c_x c_y S_{x,y}}. \tag{4.14}$$

The minimization of E in relation to $\{c_y\}$ leads to the generalized eigenvalue equation

$$\frac{\partial E}{\partial c_y} = 0 \qquad \forall y \tag{4.15}$$

$$\mathbf{H}\vec{c} = E\mathbf{S}\vec{c}. \tag{4.16}$$

Monte Carlo integration is used to evaluate H_{xy} and S_{xy}. Their elements lead to the set of coefficients $\vec{c}$ that are used to modify p_y. If one considers $|\Phi^{(1)}\rangle$ similar to $|\Psi^0\rangle$, we have $\frac{c_y}{c_0} << 1$, for $y > 0$. Thus, old coefficients might be replaced by

$$p'_y = p_y + \frac{c_y}{c_0}. \tag{4.17}$$

The new wave function can now be similarly expanded as Equation 4.8 and the procedure is iterated until the convergence criteria for energy or variance is achieved.

Nevertheless, the $\frac{c_y}{c_0}$ ratio might be large, resulting in an unstable optimization. In this case, the Hamiltonian can be modified as

$$\mathbf{H} \to \mathbf{H} + a\mathbf{A}, \tag{4.18}$$

where

$$\mathbf{A} = \begin{pmatrix} 0 & 0 & 0 & 0 & 0 & ... & 0 \\ 0 & 1 & 0 & 0 & 0 & ... & 0 \\ 0 & 0 & 1 & 0 & 0 & ... & 0 \\ . & & & . & & & . \\ . & & & & . & & . \\ . & & & & & . & . \\ 0 & 0 & 0 & 0 & ... & & 1 \end{pmatrix} \tag{4.19}$$

$\mathbf{A}$ is a matrix which adds an uniform diagonal shift, $a > 0$, on $\mathbf{H}$ elements, without affecting $|\Psi^0\rangle$. However such adjustment might not be enough, mainly because it is equal to all parameters. Thus, we can include a second adjustment,

$$\mathbf{H} \to \mathbf{H} + a\mathbf{A} + b\mathbf{B}. \tag{4.20}$$

As opposite to $\mathbf{A}$, matrix $\mathbf{B}$ modifies the elements of $\mathbf{H}$ in different ways. It accounts for corrections for the terms in which the norm of $|\Psi^x\rangle$ is larger. $\mathbf{B}$ is given by

$$\mathbf{B} = \left(\mathbf{Q}^+\right)^{-1} \mathbf{T} \mathbf{Q}^{-1}, \tag{4.21}$$

where

$$Q_{ij} = \delta_{ij} - \delta_{i0}\left(1 - \delta_{j0}\right) S_{0j} \tag{4.22}$$

and

$$T_{ij} = \left(1 - \delta_{i0}\delta_{j0}\right)\left[\mathbf{Q}^+\mathbf{S}\mathbf{Q}\right]_{ij}. \tag{4.23}$$

Successive evaluations of Ψ_T, i.e., during the wave function optimization procedure, accounts for the most costly part of the computation, so it is beneficial to start with a reasonable Ψ_T. Aiming to reduce such cost, optimization steps are grouped and correlated samplings are used, lowering the need to generate new sets of configurations at each change of the wave function [3].

4.2   Correlated Sampling

Correlated sampling can be made when two wave functions, Ψ_C and Ψ_D present similar parameters and form. It allows one to use the sampling associated to Ψ_D to estimate a trial energy E_C associated to a trial wave function Ψ_C. In this manner it is no longer necessary to generate a set of configurations associated to Ψ_C [3].

Recalling the expression to obtain E_C (Equation 4.6),

$$E_C = \frac{\int d\mathbf{r}\Psi_C\Psi_C^*\frac{H\Psi_C}{\Psi_C}}{\int d\mathbf{r}\Psi_C^*\Psi_C} = \int d\mathbf{r}P_C\left(\mathbf{r}\right)\frac{H\Psi_C}{\Psi_C} \simeq \frac{1}{N}\sum_i^N \left(\frac{H\Psi_C}{\Psi_C}\right)_i. \tag{4.24}$$

By multiplying both the numerator and the denominator, of the first identity of Equation 4.24, by $\frac{\Psi_D^*\Psi_D}{\Psi_D^*\Psi_D}$, one finds

$$E_C = \frac{\int d\mathbf{r}\frac{\Psi_C^*\Psi_C}{\Psi_D^*\Psi_D}\Psi_D^*\Psi_D\frac{H\Psi_C}{\Psi_C}}{\int d\mathbf{r}\frac{\Psi_C^*\Psi_C}{\Psi_D^*\Psi_D}\Psi_D^*\Psi_D}. \tag{4.25}$$

Then, we divide both numerator and denominator by $\int d\mathbf{r}|\Psi_D|^2$:

$$E_C = \frac{\frac{\int d\mathbf{r}\frac{|\Psi_C|^2}{|\Psi_D|^2}|\Psi_D|^2\frac{H\Psi_C}{\Psi_C}}{\int d\mathbf{r}|\Psi_D|^2}}{\frac{\int d\mathbf{r}\frac{|\Psi_C|^2}{|\Psi_D|^2}|\Psi_D|^2}{\int d\mathbf{r}|\Psi_D|^2}}. \tag{4.26}$$

The probability associated to Ψ_D, $P_D(\mathbf{r})$ - Equation 4.4, can be identified on both

numerator and denominator. Then Equation 4.26 is reduced to

$$E_C = \frac{\int d\mathbf{r} P_D(\mathbf{r}) \frac{|\Psi_C|^2}{|\Psi_D|^2} \left(\frac{H\Psi_C}{\Psi_C} \right)}{\int d\mathbf{r} P_D(\mathbf{r}) \frac{|\Psi_C|^2}{|\Psi_D|^2}}. \tag{4.27}$$

Similarly to Equation 4.6, the integral on numerador, for N large enough, is approximated to:

$$\int d\mathbf{r} P_D(\mathbf{r}) \frac{|\Psi_C|^2}{|\Psi_D|^2} \left(\frac{H\Psi_C}{\Psi_C} \right) \simeq \frac{1}{N} \sum_i^N \left(\frac{|\Psi_C|^2}{|\Psi_D|^2} \frac{H\Psi_C}{\Psi_C} \right)_i \tag{4.28}$$

and, in the denominator

$$\int d\mathbf{r} P_D(\mathbf{r}) \frac{|\Psi_C|^2}{|\Psi_D|^2} \simeq \frac{1}{N} \sum_i^N \left(\frac{|\Psi_C|^2}{|\Psi_D|^2} \right)_i. \tag{4.29}$$

Thus, E_C can be estimated using configurations sampled from $P_D(\mathbf{r})$ by

$$E_C = \frac{\sum_i^N \left(\frac{|\Psi_C|^2}{|\Psi_D|^2} \frac{H\Psi_C}{\Psi_C} \right)_i}{\sum_i^N \left(\frac{|\Psi_C|^2}{|\Psi_D|^2} \right)_i}. \tag{4.30}$$

Due to the presence of error bars in QMC results, if Ψ_C and Ψ_D are similar enough, sampling associated with ψ_D, when used to estimate quantities associated with Ψ_C, will produce correlated results. Therefore their comparison is more meaninful.

4.3   Jastrow factor

Fermionic systems require an antisymmetrized wave function. In QMC methods, Ψ_T can be written as products of Slater-Determinants with orbitals taken from DFT calculations, $\Psi_{SD}^\uparrow$ and $\Psi_{SD}^\downarrow$ for up and down spins, and correlation terms of the Jastrow form $J(r; \{p_y\})$,

$$\Psi_T = \Psi_{SD}^\uparrow \cdot \Psi_{SD}^\downarrow \cdot e^{-J(r;\{p_y\})}. \tag{4.31}$$

By writing the Slater determinant as $\Psi_{SD}^\uparrow$ and $\Psi_{SD}^\downarrow$, instead of a single determinant with both up and down spins, we no longer have an antisymmetric wave function, as we would if a single determinant was used. However, it still returns the same expectation value for spin independent operators. Such split of the determinant turns a larger one into two smaller, therefore reducing the computational cost [3]. The $J(r; \{p_y\})$ term can be written as

$$J(r; \{p_y\}) = \sum_i u_1(r_i) + \sum_{\sigma\sigma'} \sum_{i>j} u_2^{\sigma\sigma'}(r_{ij}) + \sum_{\sigma\sigma'} \sum_{i>j} u_3(r_{Ii}, r_{Ij}, r_{ij}) + ... , \tag{4.32}$$

where it is included interactions between electron-ion (one-body - u_1), electron-electron

(two-body - u_2), and electron-ion-electron (three-body - u_3) [35, 38]. In Equation 4.32, σ accounts for a spin variable.

In our calculation, the one- and two-body terms are implemented as one dimensional cubic B-spline functions [37],

$$u_i(r) = \sum_{y=0}^{M} p_y B_3 \left(\frac{r}{\frac{r_c}{M}} - y \right), \tag{4.33}$$

in which the subscript i accounts for either 1 or 2, meaning the one- and two-body terms. In addition, M comprises the number of variational parameters $\{p_y\}$, for $y \neq 0$. The parameter p_0 is determined by a cusp condition,

$$p_0 = p_2 - \frac{2M}{r_c} \left. \frac{\partial u}{\partial r} \right|_{r=0}. \tag{4.34}$$

Although u_1 could be included in Ψ_{SD}, it generally appears in the Jastrow factor. Two-body terms tend to make the electronic density uniform, increasing its value on low-density regions and vice-versa [3]. Since the electronic density originated from Ψ_{SD} is assumed to be the correct one, u_1 term is used to reestabilish such density [39].

The u_2 functions must obey certain requirements in order to accurately describe correlations for systems where the interacting potential goes to infinity in the limit the relative distance between particles goes to zero. The wave function needs to be divergent and twice diferentiable. The u_1 and u_2 derivatives must be defined at $r = 0$. These as known as Kato's cusp conditions,

$$\left. \frac{\partial u_1(r_i)}{\partial r_i} \right|_{r_i=0} = Z u_1(r_i), \tag{4.35}$$

$$\left. \frac{\partial u_2^{\sigma\sigma}(r_{ij})}{\partial r_{ij}} \right|_{r_{ij}=0} = -\frac{1}{4} u_2^{\sigma\sigma}(r_{ij}) \tag{4.36}$$

and

$$\left. \frac{\partial u_2^{\sigma\sigma'}(r_{ij})}{\partial r_{ij}} \right|_{r_{ij}=0} = -\frac{1}{2} u_2^{\sigma\sigma'}(r_{ij}). \tag{4.37}$$

As can be seen from Equations 4.36 and 4.37, u_2 terms are spin-dependent and divergence changes according to spin [40, 41].

Our VMC simulations use either up to two-body or three-body interaction terms. Regarding the three-body correlation term, the following form was used [37, 42],

$$u_3(r_{\sigma I}, r_{\sigma' I}, r_{\sigma\sigma'}) = \sum_{w=0}^{M_{eI}} \sum_{y=0}^{M_{eI}} \sum_{z=0}^{M_{ee}} p_{wyz} \cdot r_{\sigma I}^w \cdot r_{\sigma' I}^y \cdot r_{\sigma\sigma'}^z \cdot$$

$$\cdot \left(r_{\sigma I} - \frac{r_c}{2} \right)^3 \Theta \left(r_{\sigma I} - \frac{r_c}{2} \right) \cdot \left(r_{\sigma' I} - \frac{r_c}{2} \right)^3 \Theta \left(r_{\sigma' I} - \frac{r_c}{2} \right), \tag{4.38}$$

where Θ is the Heaviside step function, M_{eI} and M_{ee} consist in the maximum polynomial orders for electron-ion and electron-electron distances, respectively, p_{wyz} are the varia-

tional parameters and r are the distances between electrons or ions.

In VMC methods, the parameters $\{p_y\}$ of $J(r; \{p_y\})$ are optimized to obtain an upper-bound of the ground-state energy [34, 43].

Chapter 5

METHODOLOGY

5.1 DFT Calculations

We performed DFT calculations mainly to generate single-particle orbitals to build Slater-Determinants for subsequent Quantum Monte Carlo calculations. Initially, our choose functional was the LDA, but its cohesive energies results differed significantly from the experimental data. Thus, we decided to change it to the Perdew, Burke and Ernzerhof (PBE) [31] functional, which is a GGA, due to its successful use in previous works covering Zr-Fe systems [3, 6, 14, 15]. The results presented in the next chapter, when not mentioned otherwise, are at the PBE level of the theory. Nevertheless, we also did calculations with the Local Density Approximation and some of them are reported as well. Moreover, we also compare the results obtained at different levels of the theory , because we intend to discuss their ability in correctly reproducing experimental data. All DFT calculations were performed using the package Quantum Espresso [44].

Core electrons were replaced by NCPPs generated by the optimized method of Rappe-Rabe-Kaxiras-Joannopoulos (RRKJ) [25, 45, 46]. Valence configurations were set to [Ne] $3s^23p^63d^64s^2$, [Ar+$3d^{10}$] $4s^24p^64d^25s^2$ and $1s^1$ for iron, zirconium and hydrogen, respectively. In order to take advantage of the system periodicity, we used a plane-wave basis set to represent the valence electrons:

$$\psi(\mathbf{r}) = \exp(i\mathbf{k} \cdot \mathbf{r}) \sum_{\mathbf{G}} c_{\mathbf{G}} \exp\left(i\mathbf{G} \cdot \mathbf{r}\right), \tag{5.1}$$

where $\mathbf{k}$ corresponds to a wave vector restricted to the first Brillouin Zone (BZ) and $\mathbf{G}$ are the reciprocal lattice vectors [27]. The use of a periodic potential leads to the following relation between the wave function at two points $\mathbf{r}$ and $\mathbf{r}+\mathbf{R}_L$, where $\mathbf{R}_L$ is the unit cell lattice vector [24]:

$$\psi(\mathbf{r} + \mathbf{R}_L) = e^{i\mathbf{k} \cdot \mathbf{R}_L} \psi(\mathbf{r}). \tag{5.2}$$

In the orbitals of Equation 5.1, it is not feasible to have an infinite summation of the reciprocal lattice vectors, therefore the sum needs to be truncated at a cut-off limite value. It is known that higher $\mathbf{G}$ vectors do not contribute significantly on final energy. By increasing $\mathbf{G}$ values in the sum, resulting basis set gets more complete and the final

energy no longer depends of this quantity. Then, after the convergence is reached, we truncate Equation 5.1 in a value $\mathbf{G}_{cut}$,

$$\psi(\mathbf{r}) = \sum_{\mathbf{G}}^{\mathbf{G}_{cut}} c_{\mathbf{G}} \exp[i(\mathbf{k}+\mathbf{G}) \cdot \mathbf{r}]. \tag{5.3}$$

The corresponding kinetic energy, known as kinetic cut-off energy, K_{cut}, is given, in atomic units, by [1, 24]:

$$K_{cut} = \frac{G_{cut}^2}{2}. \tag{5.4}$$

In the code we use, one of the input parameter is K_{cut}. It will determine the number of plane waves employed in the calculations. Such number is determined through a calculation for the simulation cell of Zr_2FeH_5. Calculations proceed until the convergence criterion $\Delta E/atom \leq 1\ meV$ is reached [1, 47].

The orbitals of Equation 5.1, $\psi(\mathbf{r})$ are also functions of wave-vectors, $\mathbf{k}$. The integrals needed in the calculations are evaluated numerically in the BZ, in a discrete set of $\mathbf{k}$ vectors. Thus, the convergence related to the number of integration points needs to be checked as well [1, 24]. As one might expect, higher number of points lead to better converged results, however it increases the computational cost. In this work, k points samplying was done by Monkhorst-Pack method, in which equidistant points at each direction are employed [48].

Regarding metallic systems, it is important to remind that occupied and unoccupied orbitals are separated by the Fermi surface, which leads to discontinuities. Thus, in order to avoid higher number of k points to sample the BZ, it is necessary to employ accurate integration methods. The most used methods for this propose are called smearing methods, which through a parameter σ approximates the step function to a well-behaved one, as can be seen at Figure 5.1 [1]. In this work, we employed the MethFessel and Paxton integration method, with σ equal to 0.005 Ry [49].
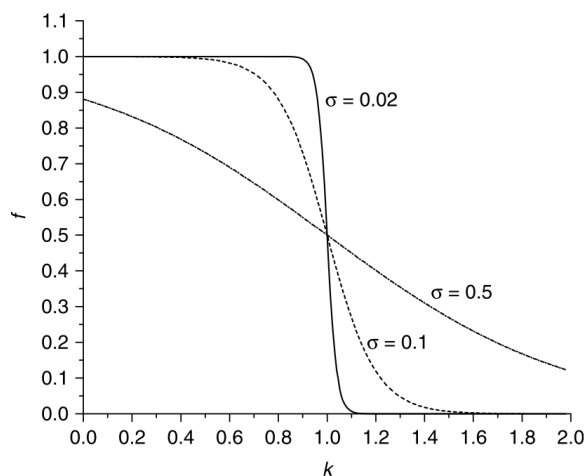
Figure 5.1: Representation of the smearing method to approximate the step function [1].

Despite our interest in crystalline systems, atomic and molecular calculations are also

required. These were performed employing the same considerations above, except for the simulation cell size. In order to avoid periodic effects, we used a large box with the atom/molecule placed in its center. We found out 20 Å length was enough to avoid such effects. For integrations at reciprocal space, a central k-point, the Γ *point* is the only one required

We performed a relaxation of the atoms, i.e., atomic positions and cell paramethers are varied until forces acting on atoms stay below 5 meV · Å^{-1}. It was done only at DFT level due to the higher QMC computational cost. Input geometries paramethers for these calculations were obtained from Inorganic Crystal Structure Database (ICSD) [50, 51, 52] and in the supplementary material of [6]. Despite the available knowledge of the experimental lattice parameters, we opted to re-optimize such simulation cells in order to check which geometries the employed methodology would predict. Then, the resulting structural parameters were compared to experimental and theoretical data, leading to an evaluation of the DFT methodology employed. Cohesive energies at both DFT and VMC levels were obtained at the optimized geometries.

5.2 VMC Calculations

QMC calculations of crystals also need to consider the periodicity of the system. However, due to the long-ranged electron-electron interactions, QMC calculations will require the use of *Supercells* (SC), i.e., integers multiples of unit cells, in order to avoid the so-called finite-size effects.

Using the BOA, the many-body electronic Hamiltonian is given by

$$H = -\frac{1}{2}\sum_{i=1}^{N}\nabla_i^2 - \sum_{\mathbf{R}_S}\sum_{A=1}^{M}\sum_{i=1}^{N}\frac{Z}{|\mathbf{r}_i - \mathbf{R}_A - \mathbf{R}_S|} + \frac{1}{2}\sum_{\mathbf{R}_S}\sum_{i<j}\frac{1}{|\mathbf{r}_i - \mathbf{r}_j - \mathbf{R}_S|}, \qquad (5.5)$$

where $\mathbf{R}_S$ accounts for the supercell lattice vectors and indices A, i and j have the same meaning as in Equation 2.2. The use of periodic boundary conditions leads to the following symmetry relation:

$$H(\mathbf{r}_1, \mathbf{r}_2, ..., \mathbf{r}_i + \mathbf{R}_S, ...\mathbf{r}_N) = H(\mathbf{r}_1, \mathbf{r}_2, ..., \mathbf{r}_N) \qquad (5.6)$$

and, similar to Equation 5.2, the wave function at $\mathbf{r}$ and $\mathbf{r}+\mathbf{L}_S$ are related by:

$$\Psi(\mathbf{r}_1, \mathbf{r}_2, ..., \mathbf{r}_i + \mathbf{R}_S, ..., \mathbf{r}_N) = e^{i\boldsymbol{\theta}\cdot\mathbf{R}_S}\Psi(\mathbf{r}_1, \mathbf{r}_2, ..., \mathbf{r}_N) \qquad (5.7)$$

where $\boldsymbol{\theta}$ is the correspondent of $\mathbf{k}$ in the SC periodicity relations.

We investigated finite-size effects by employing the following simulation cells. For Zr and Fe, we used 16- and 54- atoms SCs for each metal, since each of their primitive cells contain 2 atoms, this means $2\times2\times2$ and $3\times3\times3$ SCs, respectively. Zr_2Fe was modelled in 6- and 48-atoms simulation cells, which means its primitive cell, with 2 formation units (FU), and a $2\times2\times2$ SC (48 FU). On the other hand, its hydride's unit cell contains 4 FU, which corresponds to 32 atoms. Due to the fact the smallest possible SC, $2 \times2 \times2$,

would contain 256 atoms, we studied Zr_2FeH_5 solely in its unit cell. Finally, for Zr_3Fe, we had 16- and 48- atoms simulation cells, being its unit cell (4 FU) and a 3×1×1 SC (12 FU). The main reason to employ a 3×1×1 SC is due to Zr_3Fe unit cell geometry: this set up leads to a more symmetrical simulation cell, thus reducing finite-size effects. Similarly, the hydride Zr_3FeH_7 was investigated in its unit cell (4 FU - 44-atoms) and in a 3×1×1 SC (12 FU - 132-atoms).

Estimations for the solids were made considering 128 equilibration steps and about 262 000 producing steps, for the smaller simulation cells, i.e. the ones with 6 and 16 atoms, and roughly 65 000 producing steps, for the remaining simulation cells. For the atoms, 1024 steps were initially discarded and, approximately, 16 000 000 steps were considering for estimating the quantities of interest. This set up lead to small errors bars with a reasonable computational cost. The calculation displacement parameter Δ for the configurations was set to achieve 50 % of global acceptance. At Table 5.1, we report the value used for each calculation. For QMC calculations, the package QMCPACK was used [37].

The trial wave function we used is of the Slater-Jastrow form, where the Slater-Determinant is build by the DFT orbitals. The Jastrow factors include one- and two-body interactions, with Jastrow factors as B-splines and with 8 parameters each. In some calculations, we also included the three-body interaction, in order to study the gain in accuracy. Such term contains a total of 52 parameters: 26 for electrons with like spin and ion and the remaining for unlike spin and ion. It is important to remind we did not alter the DFT orbitals of the Slater-Determinant. During the wave function optimization procedure, only the Jastrow factor parameters were modified. Calculations for atoms required the use of open boundary conditions, we set 15 a.u. for cut-off radius.

Table 5.1: Displacement parameter Δ for the given systems.

	Zr	Zr_2Fe	Zr_2FeH_5	Zr_3Fe	Zr_3FeH_7	Fe
Δ	0.36	0.23	0.23	0.26	0.25	0.13

5.3 Determination of Cohesive Energies and Formation Entalpies

After atomic and geometry optimization calculations, we employed the following equation

$$E_{coh}^{(Zr_xFe)} = \frac{E_{sol}^{(Zr_xFe)} - xE_{atom}^{(Zr)} - E_{atom}^{(Fe)}}{x+1} \qquad (5.8)$$

in order to obtain cohesive energies , in eV/atom, for pure metals and alloys. In Equation 5.8, E_{sol} and E_{atom} accounts for the solid and atom energies, respectively. As previously mentioned, this was calculated at both DFT and VMC levels and results were compared between each other and with published data.

The formation enthalpy for a given alloy Zr_xFe is given by

$$E_{form}^{(Zr_xFe)} = (x+1)E_{coh}^{(Zr_xFe)} - xE_{coh}^{(Zr)} - E_{coh}^{(Fe)}, \tag{5.9}$$

whereas, for a hydride Zr_xFeH_y, we have

$$E_{form}^{(Zr_xFeH_y)} = (x+y+1)E_{coh}^{(Zr_xFeH_y)}+$$

$$-(x+1)E_{coh}^{(Zr_xFe)} - \frac{y}{2}E_{bin}^{(H_2)}, \tag{5.10}$$

where the last term corresponds to the hydrogen molecule binding energy and it is given by

$$E_{bind}(H_2) = E_{molec}^{(H_2)} - 2E_{atom}^{(H)}, \tag{5.11}$$

where E_{molec} is the molecule energy.

The obtained results are discussed in the next chapter of this dissertation.

Chapter 6

RESULTS

6.1 Pseudopotential Validation

It is of great importance, after the definition of the basis-set and integration methods, to verify the reproducibility of the results. In terms of the pseudotentials used, one must check its transferability, which is related to the ability of correctly reproduce the core potential at different chemical environments. Accordingly, before effectively apply the proposed methodology, we performed simple atomic calculations in order to reproduce results from the literature [45, 46], which used similar set up and the same pseudopotentials. This step is also required for the PBE functional evaluation. We calculated the first 4 ionization potentials (IP), for iron, and the 1st IP and the electron affinity (EA), for Zr.

IP is defined as the energy required to remove one electron of an atom at a given state, which could be neutral (1st IP), single positively charged (2nd IP) and so on. On the other hand, EA is the energy difference between a negatively charged and a neutral atom [53]. Results obtained at both levels of the theory (DFT and QMC) were compared to published and experimental data.

For VMC calculations, the following equations have been employed to get the Nth IP and EA values for a given local energy i:

$$IP_i^{(N)} = \left(E_{L_i}(\mathrm{A}^N) - E_{L_i}(\mathrm{A}^{N-1}) \right) \tag{6.1}$$

and

$$EA_i = \left(E_{L_i}(\mathrm{A}) - E_{L_i}(\mathrm{A}^{-1}) \right). \tag{6.2}$$

where A^N corresponds to a state with N electrons removed from atom A. Later, the mean and error bars of these quantities were calculated by blocking averages.

Iron IP results are summarised in Table 6.1. By comparing our DFT and VMC results, we can infer, except for $IP^{(1)}$, that our VMC results are comparable to experimental data, as expected. In addition, by comparing our VMC results with DMC from Ref. [45], we can see (except for $IP^{(1)}$) that our VMC calculations are in good agreement with the more accurated results from DMC. A possible explanation for the discrepancy in our calculated $IP^{(1)}$ may be the lack of a three-body correlation term in the Jastrow factor. It can thus be suggested that the neutral Fe atom presents higher correlations. It is worth mention

that VMC results from [54] employed three-body correlations.

Table 6.1: 1st to 4th IP (in eV) calculated for Fe, at DFT and VMC levels. The following three columns are results from the literature. In the last one, we report experimental data.

	This work		Mitáš et al. [54]		Krogel et al. [45]	Exp. [53]
	DFT	VMC	VMC	DMC	DMC	
IP$^{(1)}$	6.88	6.25(7)	7.61(6)	7.67(6)	7.50(4)	7.870
IP$^{(2)}$	13.87	15.94(5)	-	-	16.06(4)	16.18
IP$^{(3)}$	26.15	29.75(5)	-	-	30.41(4)	30.651
IP$^{(4)}$	48.26	55.18(5)	-	-	54.96(4)	54.8

Calculated values of the IP$^{(1)}$ and EA for Zr, presented in Table 6.2, show that our VMC results lie close to those of [46] and are in reasonable agreement with experimental values. When compared with iron IP(1), we can infer Zr presents lower correlations, thus two-body terms are sufficient to describe it. Our results and those of the literature for DFT are in agreement with each other, but far from experimental values. Results from VMC calculations are near the experimental data. We highlight the EA result, which used wave functions obtained from DFT calculations, it is in excellent agreement with the experimental datum.

Table 6.2: 1st IP and EA (in eV) calculated for Zr, at DFT and VMC levels. They are compared with theoretical values from the literature and experimental data.

	This work		Shin et al. [46]		Exp. [53]
	DFT	VMC	DFT	DMC	
IP$^{(1)}$	5.42	6.54(6)	5.03	6.43(2)	6.84
EA$^{(1)}$	1.68	0.43(6)	1.75	0.41(3)	0.426

In conclusion, these results show that the functional and methodology proposed are adequate to estimate the properties in which we are interested.

6.2 DFT Calculations

We performed DFT convergence tests in order to obtain the optimum value for the following parameters: cut-off energy and the amount of points required for the reciprocal space integrations. The convergence criteria of 1 meV (7×10^{-5} Ry) per atom was imposed for such parameters.

The basis set convergence tests were done by varying the cut-off energy at Zr_2FeH_5 unit cell, from 250 to 350 Ry and checking the absolute energy behavior. The use of NCPPs is the main reason we expect convergence to be achieved with a large basis set, when compared to USPPs [24]. The range 250 to 350 Ry was considered because we use a Norm-Conserving pseudopotential.

In Figure 6.1, we plotted relative energies, with respect to the cut-off energy at 350 Ry, as a function of the cut-off energy. From this plot, it is possible to observe that the convergence is achieved at 300 Ry, which is the value we choose for this parameter. Although

there are previous DFT studies covering Zr-Fe system and its hydrides [14, 15, 19], most of them used USPPs, what prevents a direct comparision with our cut-off energy. As already mentioned, the USPPs require much less plane-waves for convergence [24]. However, we can mention Krogel *et al.* [45] and Shin *et al.* [46] studies, where the convergence of the cut-off energy were performed considering the pseudopotentials we use in our calculations. With respect to iron, Krogel and co-authors suggest 270 Ry, whereas for Zr, Shin *et al.* used 350 Ry. Though our result lies at an intermediate point, it is important to remind Krogel *et al.* performed their convergence calculations at a pure Fe system, while Shin and co-workers worked on Zr-Hf compounds, without mentioning the convergence criteria employed.
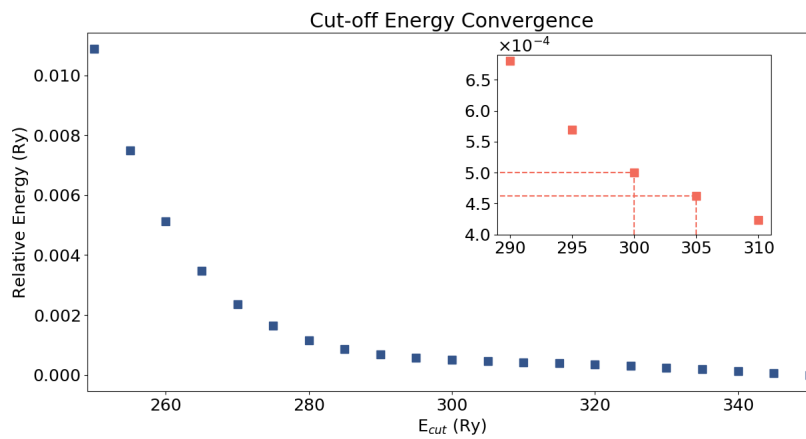
Figure 6.1: Cut-off energy convergence. The energy associated with $E_{cut} = 350$ Ry is taken as reference. In the inset, it is possible to observe when the convergence criteria is met. Please, note a change in the scale for the relative energy.

In contrast to the basis set size, the number of points in the reciprocal space required to accomplish the BZ integration is related to unit cell geometry. Thus, it is necessary to perform a test for each system under study, except for isolated atoms, since they require only the Γ point. As an example, we plot in Figure 6.2 the convergence study for the iron unit cell. In Table 6.3 our results are summarized, as well as those of previous studies.

Table 6.3: Results for k points convergence tests and comparision with values used in previous studies.

System	This work	Literature	
		Result	Convergence Criteria
hcp Zr	18 ×18 ×10	21 ×21 ×17 [55]	0.1 meV
Zr_2Fe	12 ×12 ×14	12 ×12 ×14 [6]	1 meV/atom
Zr_2FeH_5	5 ×5 ×7	6 ×6 ×8 [14]	-
Zr_3Fe	11 ×3 ×4	-	-
Zr_3FeH_7	9 ×3 ×3	10 ×3 ×3 [14]	-
bcc Fe	18 ×18 ×18	20 ×20 ×20 [15]	1 meV/atom

For Zr_2Fe, our result match the one obtained by Ali *et al.* [6]. However, there are slight variations on remaining systems, such as Zr_2FeH_5 and Zr_3FeH_7, which did not have
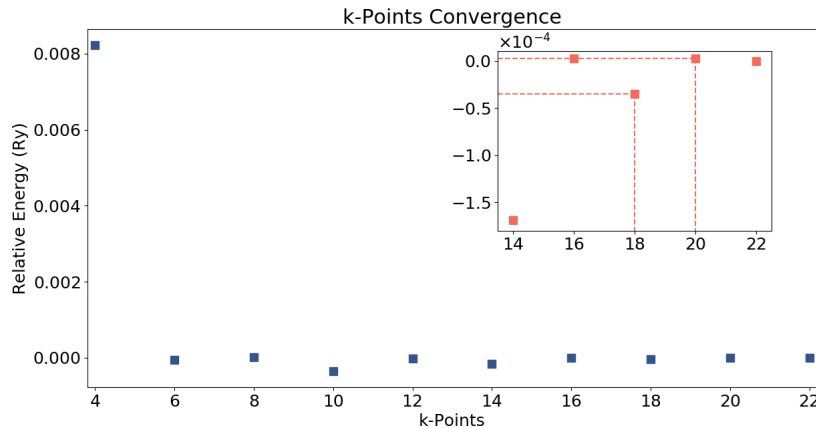
Figure 6.2: Convergence with respect to the set of k-points. The relative energy is taken into account with reference to the set with 22 k-points. In the inset, it is possible to observe details of the convergence. Please, note a change in the scale for the relative energy.

the convergence criterion reported in [14]. For the hcp Zr, the authors [55] used a tighter convergence. In [15], the same convergence criterion we use was employed.

Finally, using the estabilished set up, geometry optimizations were performed for the solid systems. In Table 6.4, we report our lattice parameter results and compare with both theoretical and experimental data. In the last column, we report the difference between our calculated values and the experimental data. From this table, it is possible to observe that our lattice optimization results are in good agreement with experimental data, where the largest difference occurs in Zr_2Fe, which is roughly 2 %.

Table 6.4: Optimized lattices parameters (in Å).

	This work	Matar [14]	Ali [15]	Shin [46]	Exp. [56, 52, 51]	Difference.
hcp Zr	$a = 3.223$	-	3.249	3.16	3.230	-0.22 %
	$c = 5.155$	-	5.176	5.15	5.144	0.21 %
Zr_2Fe	$a = 6.239$	6.250	6.276	-	6.385	-2.29 %
	$c = 5.729$	5.710	5.738	-	5.596	2.38 %
Zr_2FeH_5	$a = 6.883$	6.904	-	-	6.921	-0.55 %
	$c = 5.629$	5.646	-	-	5.620	0.16 %
Zr_3Fe	$a = 3.279$	3.29	3.310	-	3.21	2.15 %
	$b = 10.858$	10.86	10.897	-	10.966	-0.98%
	$c = 8.912$	8.93	8.940	-	8.825	0.99 %
Zr_3FeH_7	$a = 3.581$	3.505	-	-	3.577	0.11 %
	$b = 10.961$	10.95	-	-	11.021	-0.54 %
	$c = 9.739$	9.73	-	-	9.612	1.32 %
bcc Fe	$a = 2.850$	-	2.843	-	2.85	0 %

Thus far, these are results exclusively obtained by DFT calculations. In the following section, purely VMC related findings will be discussed. In the next chapter, DFT and VMC results for cohesive energies and formation enthalpies are compared.

6.3 VMC Calculations

The inclusion of Jastrow factors in the VMC calculations lead to a decrease on trial energy, as already expected. Its optimal value was obtained through the minimization method described in Chapter 4. In Figure 6.3, we have subtracted from the Zr_2Fe trial energy (simulation cell with 6 atoms), in a given optimization step, its optimal value. In the figure plot, this quantity is displayed as a function of the optimization step. This is to make clear how much energy is retrieved in the optimization process. In the inset, we can observe details of the convergence process. After convergence, differences between trial energies for different optimization steps lie bellow 3 times the uncertainty of the estimated energy. Thus, all points subsequent to the step 4 are statistically equivalent. In our calculations we choose the parameters of step 8 and its associated energy is taken as the reference. From this plot we can see that, for Zr_2Fe primitive cell (6 atoms), the inclusion of optimal correlations lead to a decrease of, approximately, 3 Ha in the trial energy.
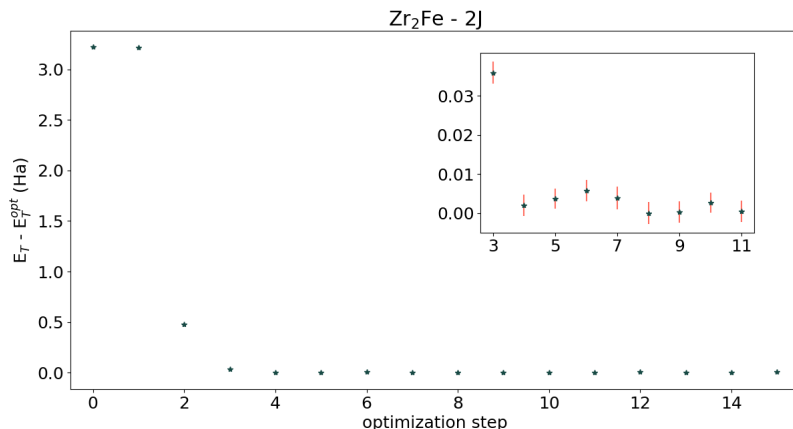
Figure 6.3: Trial energy as a function of the optimization step for Zr_2Fe subtracted from its optimal value. The trial energy in step 8 is taken as our variational optimal value.

In Table 6.5, we report, for the metallic systems, the decrease of the total energy per simulation cell (ΔE_T) and per atom (ΔE_T/atom) after the optimization of the trial wave function with the inclusion of two-body and its further reduction with three-body correlatins terms. By comparing the solids calculations, it is possible to observe a trend, in which iron seems to present a higher correlation energy, due to the higher decrease in ΔE_T/atom. Such tendency is also observed after the inclusion of the three-body correlation term and indicates that iron-related systems are highly correlated. In this case, it is important to remind that our result is an upper bound to the ground state energy and a large decrease of the trial energy might not assure that all correlated energy was recovered.

Regarding the atomic calculations, iron also presented a higher decrease on E_T than Zr. As it was stated in Section 6.1, out $IP^{(1)}$ result for Fe had a larger discrepancy, when compared to the experimental datum. This suggests that the inclusion of the two-body correlation term could recover a small fraction of the Fe atom correlation energy. We decided to perform a new calculation of iron's 1st ionization potential by including the

Table 6.5: Decrease in energy due to two-body correlations and its further decrease by introducing those of three-body at the given simulation cells sizes. The solid systems are ordered in increasing content of Fe.

System		ΔE_T (Ha)		ΔE_T/atom (Ha)	
		2-body	3-body	2-body	3-body
Zr	atomic	0.217(2)	0.0133(9)	0.217(2)	0.0133(9)
	hcp 16-atoms	7.270(5)	0.196(3)	0.4544(3)	0.0122(2)
	hcp 54-atoms	23.46(2)		0.4345(3)	
Zr_3Fe	16-atoms	7.585(8)	0.191(6)	0.4741(5)	0.0119(3)
	48-atoms	23.88(2)		0.4975(4)	
Zr_2Fe	6-atoms	3.219(4)	0.248(3)	0.5365(7)	0.0414(6)
	48-atoms	24.0(4)		0.500(8)	
Fe	bcc 16-atoms	10.24(2)	1.018(8)	0.640(1)	0.0638(5)
	bcc 54-atoms	30.1(1)		0.558(2)	
	atomic	0.920(4)	0.072(2)	0.920(4)	0.072(2)

three-body correlation term at Fe^{+1} atom as well and the obtained result was 7.1(2) eV. This is an improvement of 0.85 eV and now the VMC result is closer to the experimental result than the DFT one. However, it is about 0.7 eV below the experimental datum, which suggests the need of a more accurate description for the iron atom. It is worth mention the Ludovicy [57] study, in which dissociation energies of iron molecules were obtained with high accuracy by DMC and a full wave function optimization, i.e. not only the terms on the Jastrow factor but also the Slater-Determinant was variationally optimized.

Similarly, we report, at Table 6.5, the observed decrease in E_T for the hydrides. It is possible to observe the values of ΔE_T for Zr_3FeH_7 are comparable with its precursor alloy, at both simulation cell sizes. For these systems, we did not include the three-body term, due to its higher computational cost.

Table 6.6: Decrease in the trial energy for the hydrides due to the wave function optimization.

System		ΔE_T (Ha)	ΔE_T/atom (Ha)
Zr_3FeH_7	44-atoms	9.08(2)	0.2063(4)
	132-atoms	24.77(5)	0.1877(3)
Zr_2FeH_5	32-atoms	6.969(7)	0.2178(2)

To conclude this section, the diagrams in Figure 6.4 show trial energies for Fe and Zr neutral atoms. Here, we report our VMC results with the LDA and PBE orbitals on the trial wave function. The notation VMC_{LDA} and VMC_{PBE} was used to denote the origin of the orbitals in the Slater-Determinant. We compare our Fe result with the two-body VMC kindly supplied by Jaron Krogel. For Zr, our VMC energy is compared with the one obtained at Shin *et al.* study [46], on 2-body VMC level as well, available at the Globus dataset [58]. Both results from the literature used LDA results in the Ψ_T. In both plots values were horizontally displaced for clarity. From these diagrams, we can see that

(a) Fe^0 (b) Zr^0
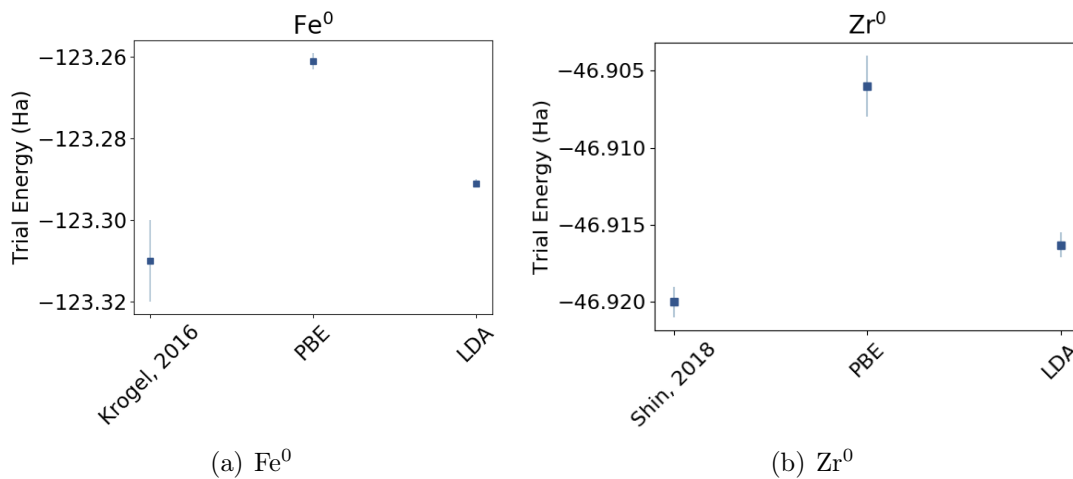
Figure 6.4: Trial energies obtained for Fe and Zr neutral atoms and comparision with previous VMC simulations. Values were horizontally displaced just for clarity.

our VMC results present a dependence in the E_{XC} functional, which is already expected, since the correlations account for a small fraction in E_T. This dependence was observed in Sola *et al.* [59] study on hcp Fe. In addition, our Zr trial energies differ by a smaller amount, roughly 0.01 Ha, whereas for Fe this difference is about 3 times larger: 0.03 Ha. By comparing our E_T, obtained with VMC_{LDA} , for both Fe and Zr calculations, with the ones of the literature, which also used the LDA, we observe they agree within 3 times the error bar.

Chapter 7

COHESIVE AND FORMATION ENERGIES

After defining the DFT set up, building the Jastrow-Slater wave function with explicit correlations terms and performing its optimization, we are now able to use atomic and solid DFT and VMC energies in order to obtain cohesive energies and formation enthalpies. As it was pointed out in Chapter 5, our energetics results obtained with the LDA differed significantly from the experimental data, prompting us to change the E_{XC} functional. Due to the high computational cost associated to a QMC calculation, simulations on larger cells were performed only for the PBE orbitals.

7.1 Cohesive Energies

In order to illustrate and discuss the cohesive energy dependence upon the E_{XC} employed, we report in Table 7.1 the DFT results obtained and comparisons with published and experimental data. It is possible to observe that all LDA results present a larger deviation in relation to the experimental data. Moreover, this is in agreement with the LDA tendency of overbinding, since all cohesive energies are larger than the experimental ones. The largest discrepancy occurs for Fe, where LDA predicts its cohesive energy to be 45 % larger than the experimental value. Similar results have been observed in previous studies, such as in Philipsen *et al.* [60] and in Hathaway *et al.* [61], in which the LDA cohesive energies were -6.25 and -6.56 eV, respectively. On the other hand, the intermetallics results presented smaller deviations than the Fe cohesive energy. Together with the fact pure Zr presented the smallest deviation in the studied series, we might conclude that the LDA seems to be inadequate to describe Fe systems.

Regarding the calculations performed with the PBE functional, as we can see in Table 7.1, results for Zr are in excellent agreement with experimental values and the associated deviations might be considered zero. Zr_3Fe and Zr_2Fe present larger, though still small, deviations from the experimental values and our results show higher or similar accuracy, when compared with a previous DFT study [15] in the same systems. Here, it is worth mention that, in Ali *et al.* study, only the sub shells 3d and 4s were treated as valence states for the iron atom, whereas our study includes the 3s and 3p states as well,

as previously mentioned. This is a strong indication that the PBE functional describes better the Fe-Zr system. In addition, our calculated cohesive energy for Fe, using the PBE functional, is close to the experimental data, when compared to the corresponding LDA result.

Table 7.1: Cohesive energies (eV), calculated with DFT, and deviations in relation to the experimental values for the given simulations cells. It is important to remind that, despite the same functional employed, in Ali *et al.* study, a different pseudopotential, with other valence configuration, was employed.

	This work				Ali *et al.* [15]	Shin *et al.* [46]	Exp.
	PBE		LDA		PBE	LDA	
hcp Zr	-6.244	-0.09%	-7.439	19%	-6.647	-7.46	-6.250
Zr_3Fe	-5.925	2.1%	-7.236	25%	-6.261	-	-5.802
Zr_2Fe	-5.800	2.4%	-7.255	28%	-6.110	-	-5.666
bcc Fe	-4.639	8.4%	-6.205	45%	-4.620	-	-4.280

Having discussed the pure DFT results, we now address those obtained with VMC and discuss how much further the dependence upon the E_{XC} functional could affect them. In Table 7.2, we report the cohesive energies obtained after the wave functions optimizations using both functionals to build the trial wave functions. For VMC_{PBE}, we include results obtained with two-body correlation terms, besides the calculated values for the different simulation cells, though we did not perform a full study about system size and finite-size effects. First, we will compare VMC_{LDA} with VMC_{PBE}, for the smaller simulation cells. After that, a brief discussion about the result depence upon the system size, i.e., the smaller and larger simulation cells, will be made.

Table 7.2: Cohesive energies (eV) and its deviations calculated with VMC. How much the computed values differ from the experimental ones (displayed in the last column) are indicated by percentages.

		VMC_{PBE}		VMC_{LDA}		Exp.
Zr	2×2×2	-6.43(2)	2.9%	-6.15(2)	-1.6%	-6.250
	3×3×3	-5.85(2)	-6.4%	-		
Zr_3Fe	1×1×1	-2.80(2)	-52%	-2.3(1)	-60%	-5.802
	3×1×1	-4.51(3)	-22%	-		
Zr_2Fe	1×1×1	-4.96(4)	-12%	-3.84(2)	-34%	-5.666
	2×2×2	-4.13(3)	-27%	-		
Fe	2×2×2	-3.26(6)	-25%	-2.40(5)	-44%	-4.280
	3×3×3	-3.1(3)	-28%	-	-	

For hcp Zr, both VMC results for the 2×2×2 SC are satisfatory and, surprisingly, LDA orbitals lead to a better result, when compared with those of PBE. Our VMC_{LDA} result is 0.1 eV above the experimental and, though it is higher than the chemical accuracy, this could be considered a good agreement, given the VMC limitations. Nevertheless, the difference between our VMC_{PBE} (for the 2×2×2 simullation cell) and the experimental result is 0.18 eV, which is also considered accurate. It is important to remind that,

although the VMC energy is an upper bound to the ground-state energy, a difference between two variational results is not, which is the case of the cohesive energy. The calculations with the 3×3×3 SC did not increase the accuracy in Zr E_{coh}, the energy increased in almost 0.6 eV. This could be related to finite-size effects in the 2×2×2, even though its result was closer to the experimental datum.

Despite which E_{XC} functional was employed to obtain the orbitals of the trial wave function, our results for 1×1×1 Zr_3Fe presented deviations of 50% and 60% in relation to the experimental value. This is a strong indication of finite-size effects, due to the fact this simulation cell is much smaller in c direction, when compared to a and b, as can be seen in Table 6.4. On the other hand, for the larger simulation cell, our VMC$_{PBE}$ optimization lead to an E_{coh} of -4.51(3) eV. Such result is 1.29 eV bellow the experimental measure, nevertheless the calculation on the 3×1×1 SC lead to an improvement of 1.71 eV in the result.

For Zr_2Fe, PBE orbitals lead to a value closer to the experimental results, when compared to LDA. For this intermetallic, we observe a larger dependence upon the E_{XC}, when compared with Zr. Similarly to Zr, calculations on a larger simulation cell lead to a decrease in the accuracy, which could also be atributted to finite-size effects in the smaller simulation cell.

For the bcc Fe, both VMC results are far from the experimental data, being the LDA the most discrepant, differing by over 40%, which is about the same absolute difference observed in the corresponding DFT calculation. On the other hand the VMC$_{PBE}$ calculation lead to a deviation of about 25% in relation to the experimental datum. Although the modest improvement, this is another indicative iron requires a higher accuracy method in order to correctly describe it.

To conclude this section, it is important to remind the Slater-Determinant contribuition in the wave function accounts for the largest part of the trial energy. In addition, it is worth mention the cohesive energy is a difference between two independent results, being its precision dependent upon both atomic and solid calculations accuracy. It is important to remind that all calculations were performed on a DFT optimized geometry, which, though resulted in very accurate parameters, also predicted slightly higher deviations in relation to the experimental data, for some cells, as we could observe in Table 6.4. Lastly, we also highlight the need to perform simulations in symmetrical cells. Zr_3Fe is an example to illustrate this, once its E_{coh} was significantly improved at the SC calculation.

7.2   Formation Energies

At Table 7.3, we show our calculated formation energies for the intermetallics. We also include previous theoretical results for comparision. Due to the better precision on the previous PBE results, we used this functional to calculate the formation energies at the DFT level.

From Table 7.3, we observe our results to lie slightly above the published theoretical ones. It is important to remember our cohesive energy results for the alloys were in a better agreement with the experimental data, when compared with the ones reported

Table 7.3: Formation energies (in kcal/mol) and comparision with the literature and the experimental data for the given intermetallics.

	This work DFT	Ali *et al.* [15]	Mukhamedov *et al.* (Zr_3Fe) Chattaraj *et al.* (Zr_2Fe)	Exp. (298 K)
Zr_3Fe	-7.626	-11.25	-11.108	-3.85
Zr_2Fe	-6.266	-9.685	-9.190	-4.89

by [15], thus such result seems to have extended to the formation energies calculations. Unfortunately our VMC results were inconclusive. From Equations 5.8 and 5.9, it is possible to observe the formation energy depends upon the solid calculations, thus larger errors might be due to the alloys or pure metals calculations, excluding the atomic results. Due to the fact our VMC results obtained for the cohesive energies presented larger deviations in relation to the experimental ones, mainly the iron-containing sytems, we believe that our main source of errors is the bcc Fe calculation.

As mentioned in Chapter 1, the enthalpy of formation of Zr_2Fe was calculated at 298 K and, in units of kcal·mol^{-1}, it is equal to -4.89 [7]. On the other hand, the theoretical results we report are for 0 K, thus the need to extrapolate them to 298 K. Both formation enthalpies are related through

$$\Delta H_{form}^{298K}(Zr_2Fe) = \Delta H_{form}^{0K}(Zr_2Fe) - 2\int_0^{298} dT C_P^{Zr}(T) -$$

$$- \int_0^{298} dT C_P^{Fe}(T) + \int_0^{298} dT C_P^{Zr_2Fe}(T), \tag{7.1}$$

where $C_P^{Zr}(T)$, $C_P^{Fe}(T)$ and $C_P^{Zr_2Fe}(T)$ corresponds to the specific heats of Zr, Fe and Zr_2Fe, respectively. In order to access the specific heat of Zr_2Fe, we used the RW-model [62], which was proposed in order to describe the behavior of the specific heat, by combining well known theoretical models with experimental data,

$$C_P(T, \Theta) = C_V^{Deb}(T) + aT + bT^2. \tag{7.2}$$

Here, a and b are fitting parameters. In this work, we used the values obtained by Saenko *et al.* [63], after a fit of their experimental measures. $C_V^{Deb}(T)$ is the specific heat in the Debye's model,

$$C_V^{Deb}(T) = 3Nk \cdot D\left(\frac{\Theta_D}{T}\right), \tag{7.3}$$

in which k is the Boltzmann's contanst and we will use N equal to 1 mol. $D\left(\frac{\Theta_D}{T}\right)$ is the Debye's function

$$D\left(\frac{\Theta_D}{T}\right) = \frac{3}{\left(\frac{\Theta_D}{T}\right)^3} \int_0^{\frac{\Theta_D}{T}} dx \frac{x^4 e^x}{(e^x - 1)^2}, \tag{7.4}$$

where Θ_D accounts for the Debye's temperature. By using the values provided in [63] for a, b and Θ_D, we are able to extrapolate the formation enthalpy of Zr_2Fe.

Moving on now to consider Zr and Fe, we decided to follow a similar procedure in order to reach an expression for its C_P. Due to the lack of previous studies in which a fitting similar to Equation 7.2 was done, we made our own fitting using experimental values of C_P and their Debye's temperatures.

According to [64], Zr Debye's temperature is equal to 291 K. We used experimental values in the range 298 to 1135 K, mostly in steps of 100 K, availale at [65]. The obtained values for a and b are listed in Table 7.4. On the other hand, the Debye's temperature for iron is 477 K [66] and we also extracted the experimental values of C_P from [65], ranging from 298 to 1000 K, in steps of 100 K. The resulting parameters are available at Table 7.4 as well.

Table 7.4: Debye's temperature (in K) and fitting parameters for solid Zr and Fe.

	$a \cdot 10^3$	$b \cdot 10^7$	Θ_D
Zr	2.25	40.23	291
Fe	4.50	305.4	477

Finally, Equation 7.1 is reduced to

$$\Delta H_{form}^{298\text{K}}(Zr_2Fe) = \Delta H_{form}^{0\text{K}}(Zr_2Fe)+$$

$$+ (-2 \times 1.344 - 1.001 + 1.741)\,\text{kcal} \cdot \text{mol}^{-1} \tag{7.5}$$

and we achieve the enthalpy of formation of Zr_2Fe at 298 K: -8.214 kcal·mol^{-1}. By comparing our DFT result with the experimental one, we observe a difference of, approximately, 3.3 kcal·mol^{-1}, a higher value when compared to the chemical accuracy (1 kcal·mol^{-1}). However it is important to remind DFT is an approximate theory and its results are subjected to the E_{XC} employed.

Regarding the intermetallic Zr_3Fe, its result should also be extrapolated to 298 K. Similarly to Equation 7.1, the following equation will be used to connect the enthalpies at different temperatures,

$$\Delta H_{form}^{298\text{K}}(Zr_3Fe) = \Delta H_{form}^{0\text{K}}(Zr_3Fe) - 2\int_0^{298} dT C_P^{Zr}(T) -$$

$$- \int_0^{298} dT C_P^{Fe}(T) + \int_0^{298} dT C_P^{Zr_3Fe}(T), \tag{7.6}$$

being $C_P^{Zr_3Fe}(T)$ given by Equation 7.2. Using the previous procedure and the fitting parameters from [67], we now have for Zr_3Fe,

$$\Delta H_{form}^{298\text{K}}(Zr_3Fe) = \Delta H_{form}^{0\text{K}}(Zr_3Fe)+$$

$$+ (-2 \times 1.344 - 1.001 + 1.51846)\,\text{kcal} \cdot \text{mol}^{-1}, \tag{7.7}$$

which leads to an enthalpy of formation, at 298 K, equal to -9.796 kcal·mol^{-1}, at DFT level. The experimental result for this alloy is -3.85 kcal·mol^{-1} [7]. Once more, it is worth

mention a DFT result is not able to achieve the chemical accuracy.

7.3 Zr-Fe Hydrides Stability

In order to study Zr-Fe hydrides, simulations with the H_2 molecule should be done. In a simillar manner as it as performed with the alloys, a prior DFT study was made in order to obtain its equilibrium geometry and to provide single-particle orbitals for the further VMC simulations. Our PBE result predicted a bond length equal to 0.75 Å, a slightly higher value when compared with its experimental value, which is 0.74 Å [68]. In addition, DFT also predicts its binding energy to be -4.54 eV. This result is about 1% bellow the experimental datum, which is -4.48 eV [69]. On the other hand, VMC optimization lead to -4.41(2) eV. Previous DMC studies [5] achieved a higher accuracy of -4.484(2), nonetheless, given the limitations of the VMC method, our result might be considered suitable. In addition, it is important to remind that the VMC calculation was performed using the DFT optimized geometry, which presents a bond length slightly higher than the experimental one.

Turning now on to the hydrides energetics, in Table 7.5, we report our calculated enthalpies of formation (at 0 K) in units of kcal·mol H_2. In this Table, we also include the theoretical predictions by Chattaraj et $al.$ [19] and the experimental measure in the incomplete hydrogen absorpition by Nobile et $al.$ [16]. To the best of our knowledge, experimental measurements or theoretical predictions for the formation enthalpy of Zr_3FeH_7 have not been published yet. The reported results for Zr_3FeH_7 were obtained at the 3×1×1 SC.

Table 7.5: Calculated formation energies for the given hydrides (in kcal·mol H_2) and comparison with the literature and the experimental data.

	This work		Chattaraj et $al.$ [19]	Exp. [16]
	DFT	VMC		
Zr_2FeH_5	-26.57	-36.7(4)	-29.98	-24.33
Zr_3FeH_7	-26.09	-21.9(5)		

From Table 7.5, we observe a better agreement between our DFT result for Zr_2FeH_5 and the theoretical one reported by Chattaraj. This observation supports the hypothesis the pure metals accounted for the greater fraction in our errors. By combining Equations 5.8-5.10, one notices the formation energy of a hydride does not rely upon the pure metals energies.

According to Nobile et $al.$ [16], Zr_2Fe reaction with hydrogen takes place at 623.15 K, therefore it is needed an extrapolation for such temperature. However, the specific heat of Zr_2FeH_5 has not been measured experimentally and we prefered to do not use the predictions made by Chattaraj et $al.$, due to the fact they were obtained through ab $initio$ simulations. Thus, we will compare our results with 0 K with the experimental value. Alike the alloys results, our DFT predictions for E_{form} present good agreement with [16], being the difference about 5.6 kcal·mol^{-1}. On the other hand, the E_{form} predicted by VMC is roughly 10 kcal·mol^{-1} H_2 above the DFT one. Futhermore, it is important to

remind our results were not extrapolated and the experimental measure, though it is in units of kcal·mol^{-1} H$_2$, corresponds to a partial absorption of H$_2$ by the alloy Zr$_2$Fe.

For Zr$_3$FeH$_7$, our calculated formation energy, at 0 K, is -26.1 kcal·mol^{-1} H$_2$, for DFT, and -21.9(8) kcal·mol^{-1} H$_2$, at the VMC level. For this reaction, there is no experimental data about its energetics or temperature of occurrence.

Chapter 8

CONCLUSIONS AND PERSPECTIVES

In addition to provide good predictions for the solids geometries, DFT calculations showed to be a good starting point for the VMC simulations. The VMC results might be made more accurate by improving trial wave functions through the introduction of higher correlation terms. It is important to remind that the cohesive energies are calculated considering an estimate made for a solid subtracted by an independent one obtained for the isolated system. Our ionization potentials and electron affinities predictions at the VMC level presented higher accuracy, when compared with the preceding DFT.

For Zr systems, correlations introduced in the wave function were less effective in lowering the trial energy, we observed small decreases in the trial energy and more accurate results. On the other hand, we observed the solids with higher ammount of iron required more correlation terms and, perhaps, a more accurate *ab initio* method, such as the DMC.

The deviations observed in the cohesive energies extended for the formation energies. On the other hand, though we did not perform an extrapolation, the estimates for the formation energies of the Zr_2FeH_5 presented a much smaller deviation in relation to the experimental measure. This is a strong indicative the pure metals calculations (mainly bcc Fe) need to be improved.

Finally, it is worth mention that most of the quantities in which we were interested are obtained by the subtraction of two computed quantities subjected to uncertainties. As a consequence, each one of the computed quantities need to be determined with high accuracy to avoid incorrect results. Additionally, since both DFT and VMC results are not "exact", we cannot discard the possibility that some of the results obtained with these methods are related to errors cancelations.

It will be highly interesting to proceed the investigations of the systems discussed in this dissertation using an "exact" method like the Difusion Monte Carlo method. This method is able to avoid some of the bias introduced by a given choice of a wave function and also consequences of a particular DFT realization.

Bibliography

[1] D. Sholl and J. A. Steckel, *Density functional theory: a practical introduction*. John Wiley & Sons, 2011.

[2] A. Lüchow and J. B. Anderson, "Monte carlo methods in electronic structures for large systems," *Annual review of physical chemistry*, vol. 51, no. 1, pp. 501–526, 2000.

[3] W. Foulkes, L. Mitas, R. Needs, and G. Rajagopal, "Quantum monte carlo simulations of solids," *Reviews of Modern Physics*, vol. 73, no. 1, p. 33, 2001.

[4] K. A. Peterson, D. Feller, and D. A. Dixon, "Chemical accuracy in ab initio thermochemistry and spectroscopy: current strategies and future challenges," *Theoretical Chemistry Accounts*, vol. 131, no. 1, p. 1079, 2012.

[5] M. Pozzo and D. Alfe, "Structural properties and enthalpy of formation of magnesium hydride from quantum monte carlo calculations," *Physical Review B*, vol. 77, no. 10, p. 104103, 2008.

[6] K. Ali, P. Ghosh, and A. Arya, "A dft study of structural, elastic and lattice dynamical properties of fe2zr and fezr2 intermetallics," *Journal of Alloys and Compounds*, vol. 723, pp. 611–619, 2017.

[7] M. Jiang, K. Oikawa, T. Ikeshoji, L. Wulff, and K. Ishida, "Thermodynamic calculations of fe-zr and fe-zr-c systems," *Journal of phase equilibria*, vol. 22, no. 4, pp. 406–417, 2001.

[8] C. Colinet, A. Pasturel, and P. Hicter, "Trends in cohesive energy of transition metal alloys," *Calphad*, vol. 9, no. 1, pp. 71–99, 1985.

[9] C. Servant, C. Gueneau, and I. Ansara, "Experimental and thermodynamic assessment of the fe zr system," *Journal of Alloys and Compounds*, vol. 220, no. 1-2, pp. 19–26, 1995.

[10] N. Rusman and M. Dahari, "A review on the current progress of metal hydrides material for solid-state hydrogen storage applications," *International Journal of Hydrogen Energy*, vol. 41, no. 28, pp. 12108–12126, 2016.

[11] R. McLellan and C. G. Harkins, "Hydrogen interactions with metals," *Materials Science and Engineering*, vol. 18, no. 1, pp. 5–35, 1975.

[12] P. Atkins, *Shriver and Atkins' inorganic chemistry*. Oxford University Press, USA, 2010.

[13] B. Sakintuna, F. Lamari-Darkrim, and M. Hirscher, "Metal hydride materials for solid hydrogen storage: a review," *International journal of hydrogen energy*, vol. 32, no. 9, pp. 1121–1140, 2007.

[14] S. F. Matar, A. F. Al Alam, D. Gédéon, and N. Ouaini, "Changes in electronic, magnetic and bonding properties from zr2feh5 to zr3feh7 addressed from ab initio," *Solid State Sciences*, vol. 25, pp. 55–62, 2013.

[15] K. Ali, A. Arya, P. Ghosh, and G. Dey, "A first principles study of cohesive, elastic and electronic properties of binary fe–zr intermetallics," *Computational Materials Science*, vol. 112, pp. 52–66, 2016.

[16] A. Nobile, W. Mosley, J. S. Holder, and K. Brooks, "Deuterium absorption and material phase characteristics of zr2fe," *Journal of alloys and compounds*, vol. 206, no. 1, pp. 83–93, 1994.

[17] F. Aubertin, S. Abel, S. Campbell, and U. Gonser, "Investigation of zr 3 fe hydride phases," *Hyperfine Interactions*, vol. 41, no. 1, pp. 543–546, 1988.

[18] W. Liu, O. D. Feya, T. T. Debela, J. R. Hester, C. J. Webb, and E. M. Gray, "Experimental and computational modelling study of ni substitution for fe in zr3fe and its hydride," *Journal of Alloys and Compounds*, vol. 781, pp. 131–139, 2019.

[19] D. Chattaraj, C. Majumder, and S. Dash, "Structural, electronic, elastic and thermodynamic properties of zr2fe and zr2feh5: A comprehensive study using first principles approach," *Journal of Alloys and Compounds*, vol. 615, pp. 234–242, 2014.

[20] A. Szabo and N. S. Ostlund, *Modern quantum chemistry: introduction to advanced electronic structure theory*. Courier Corporation, 1989.

[21] C. J. Cramer, *Essentials of computational chemistry: theories and models*. John Wiley & Sons, 2013.

[22] F. Jensen, *Introduction to computational chemistry*. John Wiley & Sons, 2013.

[23] L. Piela, *Ideas of quantum chemistry*. Elsevier, 2006.

[24] V. Brázdová and D. R. Bowler, *Atomistic computer simulations: a practical guide*. John Wiley & Sons, 2013.

[25] A. M. Rappe, K. M. Rabe, E. Kaxiras, and J. Joannopoulos, "Optimized pseudopotentials," *Physical Review B*, vol. 41, no. 2, p. 1227, 1990.

[26] D. J. Singh and L. Nordstrom, *Planewaves, Pseudopotentials, and the LAPW Method*. Springer, 2006.

[27] C. Fiolhais, F. Nogueira, and M. A. Marques, *A primer in density functional theory*, vol. 620. Springer Science & Business Media, 2003.

[28] J. C. Phillips and L. Kleinman, "New method for calculating wave functions in crystals and molecules," *Physical Review*, vol. 116, no. 2, p. 287, 1959.

[29] G. Kresse and D. Joubert, "From ultrasoft pseudopotentials to the projector augmented-wave method," *Physical Review B*, vol. 59, no. 3, p. 1758, 1999.

[30] D. Vanderbilt, "Soft self-consistent pseudopotentials in a generalized eigenvalue formalism," *Physical Review B*, vol. 41, no. 11, p. 7892, 1990.

[31] J. P. Perdew, K. Burke, and M. Ernzerhof, "Generalized gradient approximation made simple," *Physical review letters*, vol. 77, no. 18, p. 3865, 1996.

[32] J. R. Reimers, *Computational methods for large systems: electronic structure approaches for biotechnology and nanotechnology*. John Wiley & Sons, 2011.

[33] R. Canabrava, S. A. Vitiello, *et al.*, "Partícula em um poço de potencial infinito e o método variacional de monte carlo," *Revista brasileira de ensino de física*, 2003.

[34] K. P. Esler, J. Kim, D. M. Ceperley, W. Purwanto, E. J. Walter, H. Krakauer, S. Zhang, P. R. Kent, R. G. Hennig, C. Umrigar, *et al.*, "Quantum monte carlo algorithms for electronic structure at the petascale; the endstation project," in *Journal of Physics: Conference Series*, vol. 125, p. 012057, IOP Publishing, 2008.

[35] W. Schattke and R. D. Muiño, *Quantum Monte-Carlo programming: for atoms, molecules, clusters, and solids*. John Wiley & Sons, 2013.

[36] C. Umrigar, J. Toulouse, C. Filippi, S. Sorella, and R. G. Hennig, "Alleviation of the fermion-sign problem by optimization of many-body wave functions," *Physical review letters*, vol. 98, no. 11, p. 110201, 2007.

[37] J. Kim, A. T. Baczewski, T. D. Beaudet, A. Benali, M. C. Bennett, M. A. Berrill, N. S. Blunt, E. J. L. Borda, M. Casula, D. M. Ceperley, *et al.*, "Qmcpack: an open source ab initio quantum monte carlo package for the electronic structure of atoms, molecules and solids," *Journal of Physics: Condensed Matter*, vol. 30, no. 19, p. 195901, 2018.

[38] R. Jastrow, "Many-body problem with strong forces," *Physical Review*, vol. 98, no. 5, p. 1479, 1955.

[39] S. Fahy, X. Wang, and S. G. Louie, "Variational quantum monte carlo nonlocal pseudopotential approach to solids: Formulation and application to diamond, graphite, and silicon," *Physical Review B*, vol. 42, no. 6, p. 3503, 1990.

[40] R. T. Pack and W. B. Brown, "Cusp conditions for molecular wavefunctions," *The Journal of Chemical Physics*, vol. 45, no. 2, pp. 556–559, 1966.

[41] J. Krogel, *Energetics of neutral interstitials in germanium.* PhD thesis, University of Illinois at Urbana-Champaign, 2013.

[42] N. Drummond, M. Towler, and R. Needs, "Jastrow correlation factor for atoms, molecules, and solids," *Physical Review B*, vol. 70, no. 23, p. 235119, 2004.

[43] W. D. Parker, J. W. Wilkins, and R. G. Hennig, "Accuracy of quantum monte carlo methods for point defects in solids," *physica status solidi (b)*, vol. 248, no. 2, pp. 267–274, 2011.

[44] P. Giannozzi, S. Baroni, N. Bonini, M. Calandra, R. Car, C. Cavazzoni, D. Ceresoli, G. L. Chiarotti, M. Cococcioni, I. Dabo, *et al.*, "Quantum espresso: a modular and open-source software project for quantum simulations of materials," *Journal of physics: Condensed matter*, vol. 21, no. 39, p. 395502, 2009.

[45] J. T. Krogel, J. A. Santana, and F. A. Reboredo, "Pseudopotentials for quantum monte carlo studies of transition metal oxides," *Physical Review B*, vol. 93, no. 7, p. 075143, 2016.

[46] H. Shin, A. Benali, Y. Luo, E. Crabb, A. Lopez-Bezanilla, L. E. Ratcliff, A. M. Jokisaari, and O. Heinonen, "Zirconia and hafnia polymorphs: Ground-state structural properties from diffusion monte carlo," *Physical Review Materials*, vol. 2, no. 7, p. 075001, 2018.

[47] C. Pisani, *Quantum-mechanical ab-initio calculation of the properties of crystalline materials*, vol. 67. Springer Science & Business Media, 2012.

[48] H. J. Monkhorst and J. D. Pack, "Special points for brillouin-zone integrations," *Physical review B*, vol. 13, no. 12, p. 5188, 1976.

[49] M. Methfessel and A. Paxton, "High-precision sampling for brillouin-zone integration in metals," *Physical Review B*, vol. 40, no. 6, p. 3616, 1989.

[50] P. Matkovic, T. Matkovic, and I. Vickovic, "The crystalline structure of the intermetallic compound fezr sub 3," *Metalurgija*, vol. 29, no. 1, pp. 3–6, 1990.

[51] V. Yartys, H. Fjellvåg, B. Hauback, A. Riabov, and M. Sørby, "Neutron diffraction studies of zr-containing intermetallic hydrides with ordered hydrogen sublattice. ii. orthorhombic zr3fed6. 7 with filled re3b-type structure," *Journal of alloys and compounds*, vol. 278, no. 1-2, pp. 252–259, 1998.

[52] V. Yartys, B. Hauback, A. Riabov, *et al.*, "Neutron diffraction studies of zr-containing intermetallic hydrides with ordered hydrogen sublattice. i. crystal structure of zr2fed5," *Journal of alloys and compounds*, vol. 274, no. 1-2, pp. 217–221, 1998.

[53] D. R. Lide, *CRC handbook of chemistry and physics: a ready-reference book of chemical and physical data.* CRC press, 1991.

[54] L. Mitáš, "Quantum monte carlo calculation of the fe atom," *Physical Review A*, vol. 49, no. 6, p. 4411, 1994.

[55] F. Wang and H. Gong, "First principles study of various zr–h phases with low h concentrations," *International journal of hydrogen energy*, vol. 37, no. 17, pp. 12393–12401, 2012.

[56] P. Villars and L. Calvert, "Pearson's handbook of crystallographic data for intermediate phases," *American Society of Metals, Cleveland, OH*, 1985.

[57] J. Ludovicy, K. H. Mood, and A. Luchow, "Full wave function optimization with quantum monte carlo—a study of the dissociation energies of zno, feo, feh, and crs," *Journal of chemical theory and computation*, vol. 15, no. 10, pp. 5221–5229, 2019.

[58] H. Shin, A. Benali, Y. Luo, E. Crabb, A. Lopez-Bezanilla, L. E. Ratcliff, A. M. Jokisaari, and O. Heinonen, "Dataset for zirconia and hafnia polymorphs – ground state structural properties from diffusion monte carlo," 2018.

[59] E. Sola, J. Brodholt, and D. Alfè, "Equation of state of hexagonal closed packed iron under earth's core conditions from quantum monte carlo calculations," *Physical Review B*, vol. 79, no. 2, p. 024107, 2009.

[60] P. Philipsen and E. Baerends, "Cohesive energy of 3d transition metals: density functional theory atomic and bulk calculations," *Physical Review B*, vol. 54, no. 8, p. 5326, 1996.

[61] K. Hathaway, H. Jansen, and A. J. Freeman, "Total-energy local-spin-density approach to structural and electronic properties of ferromagnetic iron," *Physical Review B*, vol. 31, no. 12, p. 7603, 1985.

[62] S. Ringberg, "Thermodynamic models and data for pure elements and other end-members of solutions," *Calphad*, vol. 19, no. 4, pp. 437–447, 1995.

[63] I. Saenko, A. Kuprava, A. Udovsky, and O. Fabrichnaya, "Heat capacity measurement of zr2fe and thermodynamic re-assessment of the fe–zr system," *Calphad*, vol. 66, p. 101625, 2019.

[64] G. Kneip Jr, J. Betterton Jr, and J. Scarbrough, "Low-temperature specific heats of titanium, zirconium, and hafnium," *Physical Review*, vol. 130, no. 5, p. 1687, 1963.

[65] I. Barin, *Thermochemical Data of Pure Substances*. John Wiley & Sons, 1995.

[66] G. Stewart, "Measurement of low-temperature specific heat," *Review of Scientific Instruments*, vol. 54, no. 1, pp. 1–11, 1983.

[67] B. Mukhamedov, I. Saenko, A. Ponomareva, M. Kriegel, A. Chugreev, A. Udovsky, O. Fabrichnaya, and I. Abrikosov, "Thermodynamic and physical properties of zr3fe and zrfe2 intermetallic compounds," *Intermetallics*, vol. 109, pp. 189–196, 2019.

[68] R. L. DeKock and H. B. Gray, *Chemical structure and bonding.* University Science Books, 1989.

[69] B. Bransden and C. Joachain, "Physics of atoms and molecules," 1983.

[70] M. H. Kalos and P. A. Whitlock, *Monte carlo methods.* John Wiley & Sons, 2009.

Appendix A

The Metropolis Algorithm

The Metropolis Algorithm, which is used during a VMC calculation, is described, in a simplified manner and for one coordinate, in the diagram bellow [33].
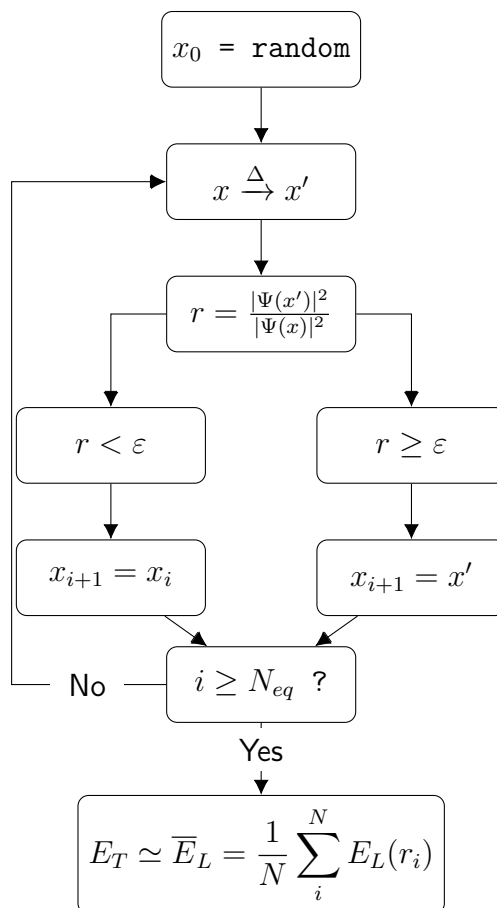
Figure A.1: Flowchart for the Metropolis algorithm.

The starting point is a random configurantion, for the particle position, x_0, for which it will be proposed a step, leading to a new configuration x'. Such proposal might be accepted or rejected (steps 3 and 4 of the algorithm), according to the ratio between the wave function amplitudes in the proposed and currently configuration. In step 4, ϵ is a random number, between 0 and 1, generated in each cicle of the algorithm. If the

proposed move is accepted, x' becomes the new configuration in the procedure. Otherwise, the previous configuration is kept. Regardless whether the proposed configuration is accepted or not, the energy can be evaluated. The proposal in step 2 depends upon a fixed displacement parameter Δ, which measures the size of the configuration moviment. Large values of Δ are not desirable, because, in most of the time, the proposed configuration will be rejected, resulting in a bad exploration of the configurational space. On the other hand, if Δ is extremely small, the configuration might remain in a region were the the wave function presents high amplitude, thus the configurational space will also not be effectively explored. In general, the value of Δ must be ajusted in order to achieve a total acceptance ratio of 40 - 60% [33, 35].

In order to turn possible an statistical analysis of the final result, there are two main points of concern before averages are performed. Returning to step 2, we observe configurations x_i and x_{i+1} are correlated through the movement proposal. In this case, such points cannot be treated as statistically independent, unless the correlation is removed. In order to do so, a given number of movement proposals, refered as *sub-steps*, are performed, between two local energies evaluations, in order to turn these values uncorrelated. The second issue is related to the results reproducibility. Due to the fact the algorithm starts from a random generated configuration, the final result should not be dependent upon such random vale. Therefore, initial configurations are discarded as well, and their local energies are not evaluated. This procedure is commonly denoted as thermalization [33, 35]. The number of discarded configurations will vary for each system, although it usually stands between 10 to 20 % of the total number of configurations. One manner to define such value is to plot the local energy as a function of the iteraction cicles and check qualitatively where convergence is achieved [70].

For a sufficient large number of samplings, the trial energy is estimated through the arithmetic mean of the local energies

$$E_T \simeq \overline{E}_L = \frac{1}{N} \sum_i^N E_L(r_i), \tag{A.1}$$

where r_i stands for a configuration in which the local energy has been evaluated. In addition, variance,

$$\sigma^2 = \frac{1}{N-1} \sum_i^N \left[E_L(r_i) - \overline{E}_L \right]^2 = \frac{1}{N-1} \left[\overline{E_L^2} - \left(\overline{E}_L \right)^2 \right], \tag{A.2}$$

and related error, $\sigma = \sqrt{\sigma^2}$, should be computed as well. However, in order to obtain a statistically meaningful error bar, it is employed the *blocking averages* procedure. Instead of performing an unique average calculation, Equation A.1 is often splitted into smaller blocks and the mean is partially evaluated for each of them,

$$E_B = \frac{1}{N_B} \sum_j^{N_B} E_L(r_j), \tag{A.3}$$

where N_B accounts for the number of local energy values in the block. In sequence, trial

energy is obtained through the average of the blocks averages,

$$E_T = \frac{1}{N_{blocks}} \sum_{k}^{N_{blocks}} (E_B)_k \,, \tag{A.4}$$

with N_{blocks} equal to the number of blocks employed. Finally, variance is computed for this result

$$\sigma^2 = \frac{1}{N-1} \left[\overline{E_B^2} - \left(\overline{E}_B \right)^2 \right] . \tag{A.5}$$

This procedure assures a final result with a reliable variance, without affecting the trial energy value [33].